4. Nanofibers of N,N,N-trimethyl chitosan capped bimetallic nanoparticles

This research specifically addresses the issue of antimicrobial resistance, which is one of the top 10 global public health threats. More specifically, it focuses on the problem of MDR microbial infected wound. The synthetic antimicrobial agents currently available in the market no longer have a significant effect on these MDR microbes. Additionally, prolonged use of antimicrobial agents leads to the development of resistance in the microbes. Given the insufficiency of efficient antibiotics, metallic nanoparticles have been used as an alternative.

In this study, primarily TMC capped gold-silver nanoparticles (Au-Ag-TMC-NPs) were reported first time for antimicrobial wound dressing and *in vivo* wound healing activity. Secondly, Au-Ag-TMC-NPs were encapsulated for the first time within a polyvinyl alcohol and chitosan-based nanofiber matrix (Au-Ag-TMC-NPs-NFs) for potential *in vivo* wound healing applications. Treating microbial resistant wounds with low or no adverse effects has proven to be a challenging task. In an effort to address this issue, we have developed Au-Ag-TMC-NPs-NFs for *in vivo* wound healing applications. Initially, developed Au-Ag-TMC-NPs were characterized for particle size, zeta potential, poly dispersity index, surface morphology, and elemental analysis. Notably, Au-Ag-TMC-NPs antimicrobial activity against MDR strains of *E. coli.*, *P. aeruginosa*, *S. aureus* and *C. albicans* were evaluated through *in vitro* experiments in comparison to the marketed broad-spectrum antibiotic. Additionally, the antimicrobial mode of action of Au-Ag-TMC-NPs was examined for anti-efflux pump activity by employing gene expression profiling. Moreover, the molecular mechanism of accelerated wound healing was explained by signaling pathway protein expression levels. The Au-Ag-TMC-NPs were evenly dispersed into Au-Ag-TMC-NPs-NFs matrix by using the process of electrospinning. The nanofibers were then applied on MDR microbes-infected mice wound sites. The wound healing

potency of nanofibers was assessed by the wound closures, re-epithelization, wound marker protein expression levels and ultrasound/photoacoustic imaging. Likewise, the real time wound visualization, angiogenesis, vascularity, and wound oxygen saturation were also evaluated. A schematic representation of the objective, specific aims and postulated hypothesis of the present work is shown in **Figure 4.1.**

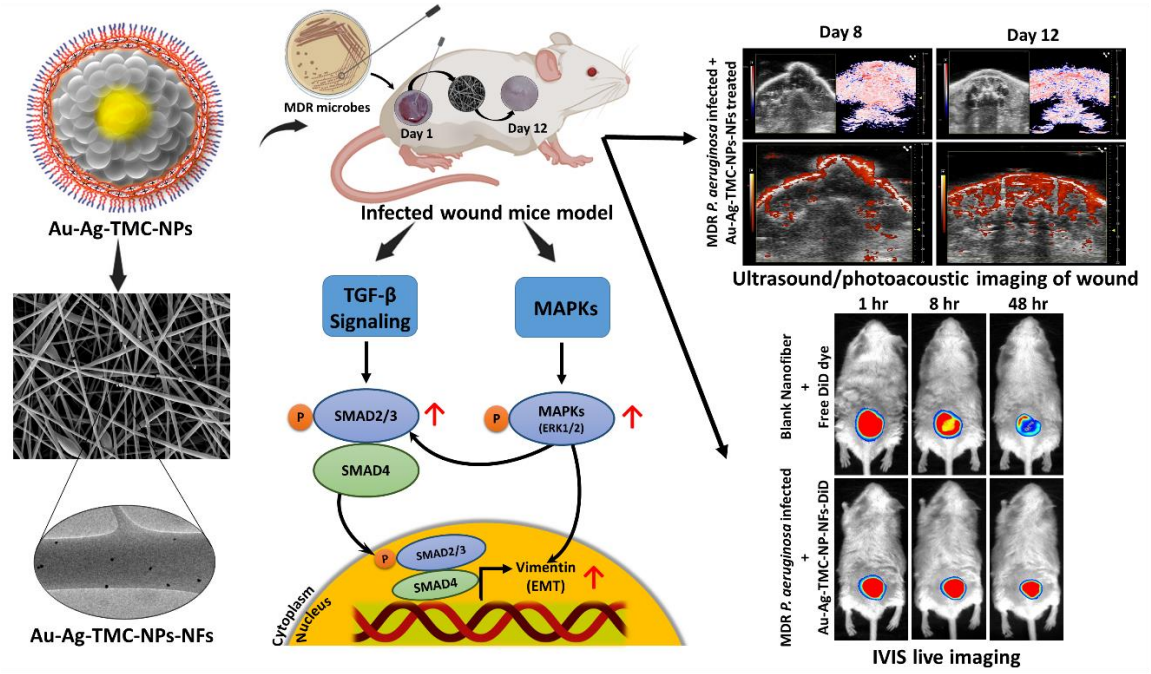

Figure 4.1. Schematic representation of objectives and hypothesis

4.1. Materials

Gold (III) chloride trihydrate (HAuCl4 ·3H2O) and silver nitrate (AgNO3), N,N,N-trimethyl chitosan $(C9H18ClNO4)_n$ (low molecular weight, degree of quaternization >50 %), polyvinyl alcohol $(C2H4O)_n$, and tween 80. Chitosan (MW ~ 30 kDa, degree of deacetylation ≥90 %) was procured from Sisco Research Laboratory Pvt. Ltd. Microbiological media (Muller Hinton broth (MHB) and Muller Hinton agar (MHA) medium) was bought from HiMedia Laboratories, Pvt. Ltd. India. LIVE/DEAD BacLight Bacterial Viability Kit (L7012) was purchased from Molecular Probes, Invitrogen (Grand Island, NY, USA). DiD'dye (DiIC18 (5) oil (1,1'-Dioctadecyl-3,3,3′,3'-

Tetramethylindodicarbocyanine Perchlorate)) was purchased from Thermo Fisher Scientific, Mumbai, India. β-Actin (13E5) Rabbit mAb (45 kDa), Vimentin (D21H3) XP® Rabbit mAb (57 kDa), Phospho-p44/42-MAPK-(Erk1/2)-(Thr202/Tyr204) (D13.14.4E) XP® Rabbit mAb (44, 42 kDa) were bought from Cell Signaling Technology (Beverly, MA). TGF-β1 polyclonal antibody (44 kDa) (Cat. No.:E-AB-33090) was purchased from Elabscience Biotechnology (USA). All the chemicals used in the present research were of analytical grade.

4.2. Methods

4.2.1. Synthesis and characterization of Au-Ag-TMC-NPs

The synthesis of gold-silver core-shell nanoparticles will be carried out using a seeded growth synthesis approach, where Au nanoparticles will be utilized as the seed material [24]. Concisely, pre-synthesized 1 ml (1 mg/ml) gold nanoparticles subjected into 9 ml of distilled water at 80°C. Varying molar ratios of HAuCl4·3H2O and AgNO3 (1:0.5, 1:1, 1:2 and 1:3) and concurrently 0.1 % 10 ml of TMC solution (as reducing and capping agent) were placed and maintained on a magnetic stirrer at 80°C. The solution colour changes from pink to dark brown within 20–25 min supporting the formation of Au–Ag nanoparticles. An additional hour was allocated for the completion of the reaction. Followed by the conjugation with TMC in the presence of resuspending agent (Tween80) to avoid particle clustering during purifying process. In brief, 5 ml (2 mg/ml) TMC aqueous solution of 1 % (w/v) Tween-80 was formulated in distilled water. Following that, 1.8 ml (1 mg/ml) of Sodium tri-poly-phosphate (TPP) solution (pH 8) was gently subjected drop wise to the solution of TMC (pH 6) while stirring at 37°C, resulting in a final pH of roughly 7 **(Figure 4.2.)**. To accomplish a comparative analysis of the antibacterial properties shown by Au-Ag-TMC-NPs, an additional five formulations were prepared as gold nanoparticles (Au-NPs), TMC based gold nanoparticles (Au-TMC-NPs), silver nanoparticles (Ag-NPs),

TMC based silver nanoparticles (Ag-TMC-NPs), and gold-silver nanoparticles (Au-Ag-NPs). Nano formulation of various batches are presented in table 4.1.

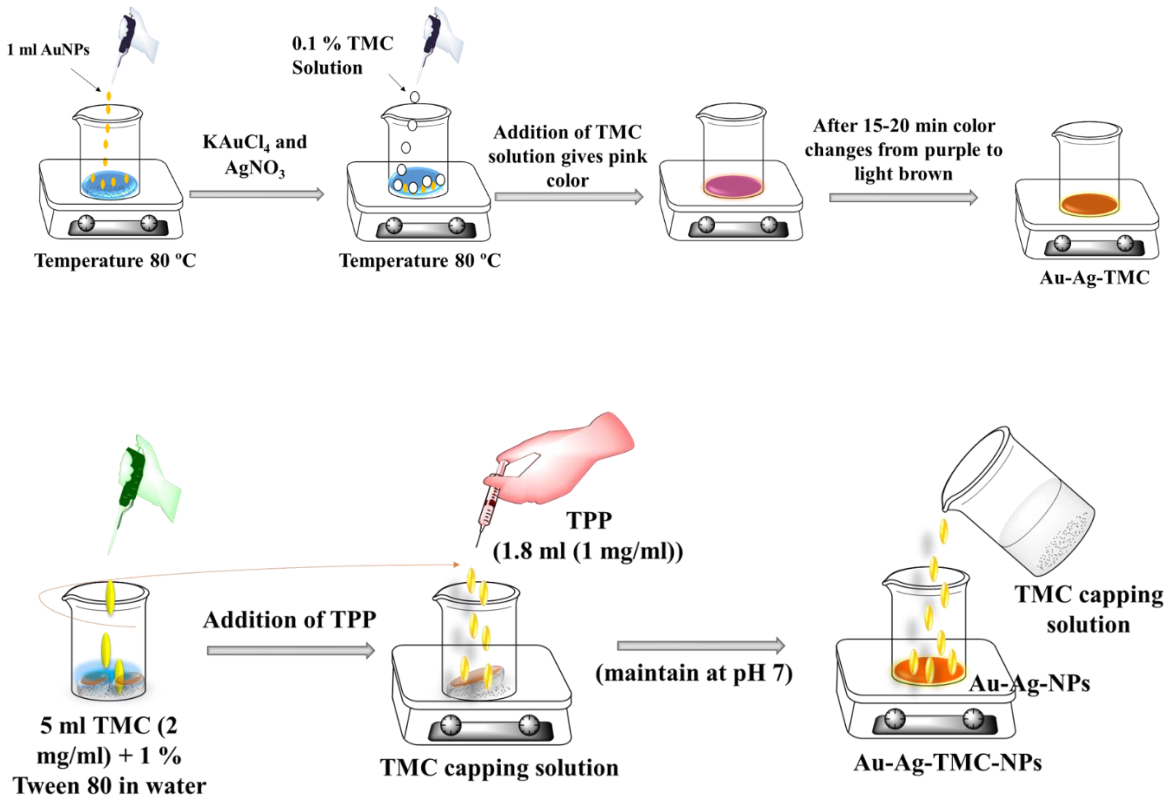

Figure 4.2. Step-wise procedure of the synthesis of Au-Ag-TMC-NPs

Table 4.1. Formulation of various batches of nanoparticles

Batches	$AgNO_3$ 10mM (ml)	$HAuCl_4$ 10mM (ml)	Gold Seed (ml)	Ascorbic Acid 50mM (ml)	TMC 0.1% (ml)	TMC 2mg/ml (ml)	Na-TPP 1mg/ml (ml)	Tween 80 1%w/v (ml)
Au-NPs	-	1	-	0.8	-	-	-	-
Au-TMC-NPs	-	1	-	-	7	5	1	1
Ag-NPs	2	-	-	1	-	-	-	-
Ag-TMC-NPs	2	-	-	-	10	4	0.5	0.7
Au-Ag-NPs	3	1	1	1.5	-	-	-	-
Au-Ag-TMC-NPs	3	1	1	-	10	5	1.8	2

4.2.1.1. Particle size, poly-dispersity index, and surface charge

The hydrodynamic particle size (PS), poly dispersity index (PDI) of the optimized nanoparticles by using the principle of dynamic light scattering was assessed using the Malvern Zetasizer (Nanoseries). Whereas surface charge was measured by electrophoretic light scattering principle.

4.2.1.2. UV-spectroscopy

The UV–visible spectra of all batches of optimized nanoparticles were obtained using a spectrophotometer (Shimadzu-1800). The UV–Visible absorbance spectra was measured by scanning the nanoparticles in the wavelength range of 300–700 nm [122]. The instrument's spectral bandwidth was adjusted to 1/10 of the scanning rate, was of 1200 nm/min.

4.2.1.3. Transmission electron microscopy analysis

The investigation of the shape, size and morphology of the optimized nanoparticles at nanoscale was conducted by TEM analysis (Tecnai G2 20 TWIN). The specimens were made using the drop-casting technique, without the utilisation of staining agents. The nanoparticles that had been optimized were subjected to sonication for a duration of 5 min. Subsequent to their dilution in distilled water. A liquid droplet was deposited onto a TEM grid made of carbon-coated copper with a mesh size of 400. The droplet was allowed to dry for an extended period of time before being subjected to examination [123].

4.2.1.4. Atomic force microscopy analysis

The investigation of the optimized nanoparticles form and morphology was conducted using AFM (NT-MDT Service & Logistics Ltd). The specimens were prepared following dilution with ultrapure water. Following a sonication period of 5 min., a small number of prepared samples was placed onto a microscope slide measuring 1 × 1 cm and subsequently allowed to dry for a duration of 24 h. The NOVA programme, developed by NT-MDT, was

utilized for image processing in order to acquire 2D and 3D AFM pictures of the optimized nanoparticles.

4.2.1.5. STEM-EDX analysis

The Au-Ag-TMC-NPs were subjected to investigation using Energy Dispersive X-ray investigation (EDX) to identify the constituent components.

4.2.2. Antimicrobial activity

4.2.2.1. Isolation of multidrug-resistant microorganism

Strain of multidrug-resistant gram-negative bacteria *E. coli.* and *P. aeruginosa*, gram-positive bacteria *S. aureus* and gram-positive fungus *C. albicans* were isolated from environmental samples and waste of Sir Sunderlal Hospital, BHU, Varanasi, Uttar Pradesh, India and other local hospitals. The selected strains were then subjected to an overnight incubation in Luria–Bertani (LB) medium at 37°C to facilitate their complete growth and confirmed by measuring the absorbance at λmax of 550 nm after centrifuging the samples at 5000 rpm for 12 min. In each experiment, a single colony of multidrug resistant bacteria was picked from the agar plate and cultured at 37°C, 200 rpm for 12 h in LBmedium [124, 125].

4.2.2.2. Estimation of MIC, MBC and MFC

Minimum inhibitory concentration (MIC) is the lowest concentration of an antimicrobial agent that prohibits observable growth of bacteria, confirming the drug's capacity to suppress microbial proliferation. Meanwhile, minimum bactericidal concentration (MBC) and minimum fungicidal concentration (MFC) is the lowest concentration of an antibiotic and antifungal that causes in the death of a specific percentage of bacterial and fungal cells, demonstrating the agent's potential to kill the bacteria and fungus rather than only prevent their development. All the optimized nanoparticles were subjected for the determination of MIC, MBC, and MFC against the strains of gram-positive and gram-negative microbial

strains (each containing 107–108 CFU/ml microbe) in a 96- well culture plates. Microbial strains introduced into a liquid broth medium of different concentrations of all the optimized nanoparticles (200 μg ml^{-1} -0.097 μg ml^{-1}) by using 2-fold serial dilution method. The values of MIC were determined by assessing the minimal concentration of the optimized nanoparticles which effectively inhibits bacterial cell proliferation. The use of the MBC and MFC serves as a valuable adjunct to the MIC assay. The objective of this research was to evaluate the minimum concentration of the formulations required to decrease the viability of the original bacterial and fungal inoculum to 100 %.

4.2.2.3. Disc diffusion assay

The experiment of disc diffusion assay was used to evaluate the antimicrobial susceptibility of the optimized nanoparticles against both grams' microbial strains. Mueller Hinton agar plates have been made by spreading the Mueller Hinton Broth cultured microbial media. The sterile Whatman paper (grade-1) of 5 mm discs' diameter were saturated with optimized nanoparticles and a standard antibiotic (Ciprofloxacin). These discs were then carefully placed onto the surface of separate MHA plates containing strains of both grams' microbial strains using sterilized forceps. The plates were subsequently incubated at a temperature of 37°C for an overnight period. The ZOI was measured in diameter (mm) by using conventional measuring scale. This was done to evaluate the resistance and compare the effectiveness of all optimized nanoparticles with the standard medication.

4.2.2.4. Anti-biofilm activity

To evaluate the anti-biofilm efficacy of the optimized nanoparticles against the microbial strains, glass slides measuring 1.3 cm2 were utilized as a substrate for the drop-casting biofilm deposition (200 μg ml^{-1} –0.097 μg ml^{-1}). The dispersion undergoing dripping was subjected to a drying process for a duration of 24 h at a temperature of 37°C, which was then followed by an additional hour of drying at a temperature of 70°C. The biofilm of the

bacterial strain that was not subjected to any treatment was used as the control in the experiment. The shape of bacterial biofilm treated with optimized nanoparticles was investigated using SEM using the MA15/18 model from Carl Zeiss Microscopy Ltd[126, 127] . In each well of a 12 well culture microplate with a round coverslip, 500 µl of a bacterial cell culture in log phase and 500 µl of different amounts of test chemicals (specifically optimized nanoparticles) were introduced. The round coverslips underwent a washing process using phosphate buffer saline (PBS) and were then fixed with a glutaraldehyde solution of 2.5 % for a duration of 3 h at a temperature of 4°C. Prior to this fixation step, the coverslips were incubated at a temperature of 37°C for a period of 24 h. The biofilm adhered to the round coverslip was then introduced to dehydration at a 4°C for 10 min., using an ethyl alcohol gradient with progressively rising concentrations (25 %, 50 %, 70 %, 90 %, and 100 %, respectively). Prior to conducting SEM analysis, the round coverslips underwent a drying process and were afterwards protected with a layer of carbon by utilizing sputter coating technique.

4.2.2.5. Live dead cell viability assay

The confocal laser scanning microscopy (CLSM) technique was used to investigate the microbial viability test. The objective is to ascertain the proportion of viable and non-viable cells by utilizing the LIVE-DEAD Bac-Light microbial viability gear [128]. As per the guidelines outlined in the Bac-Light™ microbial viability gear user manual, the mixture of stain was administered in one of three ways: (1) directly applied to surfaces covered with biofilm, where the stain mix was diluted with PBS and pipetted onto the surfaces, subsequently shielded with a coverslip; (2) applied to microbial cells taken off from the surfaces utilizing ultrasonography; or (3) applied to microbes collected from the upper layer of the microbial biofilms. The stained samples underwent incubation for a duration of 15 min. at ambient temperature under conditions of darkness.

4.2.2.6. TEM microscopy of microbes

TEM is a potent technique used to examine the structural properties, internal organization, and interactions of microbes with their surrounding environment. The microbial cells in the control group (untreated) and the group treated with Au-Ag-TMC-NPs (optimized concentration for the respective microbe) were subjected to two washes with PBS (pH 7.4). Afterward, they were fixed with 2.5% (v/v) glutaraldehyde, subsequent to post-fixation using 1% osmium tetraoxide. Finally, the cells were then washed again with PBS (pH 7.4) [129]. Moreover, the specimens underwent a slow dehydration process with the progressive augmentation of ethanol concentration. The thin slices were prepared with an ultra-microtome instrument (Leica; model- UC7) equipped with a diamond knife, followed by subsequently affixed onto copper grids [130]. The sections above were promptly analyzed following their preparation utilizing TEM with cryogenic capabilities (CRYO-TEM (TALOS S), Thermo Scientific) operating at an accelerating voltage of 80 Kilovolts.

4.2.2.7. Atomic force microscopy of microbes

The acquisition of AFM pictures was performed on cells that were placed onto glass slides (NTEGRA Prima-NT-MDT Service & Logistics Ltd). When it comes to analysing the biochemical and material aspects of filamentous structures formed by live bacterial cells in aqueous environments, AFM is an effective tool [131]. A micro cantilever with a sharp probing tip at its end is used to do horizontal line scans across a surface. When the cantilever's tip makes contact with a surface, it causes the device to bend, producing a topographic map. Sub-molecular resolution nano-scale topographical pictures of surface features under physiological circumstances and with little sample preparation are achieved. The microbial cells used for AFM imaging were cultivated on surfaces that had been pre-treated with Au-Ag-TMC-NPs (optimized concentration for the respective microbe) at time interval of 0 hr, 06 hr and 12 hr, followed by washing with PBS for 24 h at 37°C, before

AFM imaging, Microorganisms that exhibited poor adhesion to the glass surface were subjected to thorough rinsing using a generous amount of milli-Q water. Subsequently, they were air-dried in a controlled atmosphere with a relative humidity of 30%. The experiment used silicon nitride cantilevers (Olympus AC240TS) with specific parameters. The cantilevers were operated at a scan speed of 1 Hz, with a frequency of resonance ranging from 80 to 100 kHz. Additionally, the cantilevers had a curvature radius of 30 nm and a stiffness value of 5 N/m [132].

4.2.2.8. Efflux pump gene expression profiling by semi-quantitative analysis (RTPCR)

Semi-quantitative RT-PCR was performed using extracted RNA from microbial isolates were cultured in the presence of a sub-inhibitory optimized concentration of nanoparticles for respective microbe as well as an untreated negative control. RNA was extracted using the QIAamp RNeasy mini gear (Qiagen GmbH, Germany) manuals provided by the manufacturer. RNA isolation was assessed for integrity via agarose gel electrophoresis. The cDNA product obtained from reverse transcription of the RNA was subjected to semi-quantitative PCR analysis was initiated with a denaturation step of 100°C for 2 min, followed by 20 cycles of 60 secs each for denaturation at 94°C, annealing at 56°C for 20 secs, and extension at 72°C for 1 min, with the last extension at 80°C for 10 min. Primer sequences were specific to the genes coding for the main efflux pump of the microbes shown in table 1 and were designed using Primer3 software and the PCR products were visualized under UV light on a 1.2% (w/v) agarose gel. All gene expressions were compared to the expression of the *ampC* gene, which was used as a housekeeping gene [133, 134]. The genBank accession numbers for the used primers are as follow *acrA*: HQ833334 [135]; *acrB*: MT956578 [136]; *MexA*: ON920994 [137]; *MexB*: NC002516 [138]; *norA*: CP011526 [139]; *norB*: MN013174 [140]; *ERG11*: XM711729 [141]; *TAC1*:

OQ383350 [142]; ampC: ON920993 [143] **(Table 4.2)**. Quantification of the PCR products was done densitometrically using Image J software.

Table 4.2. Primers used in semi-quantitative RT-PCR

Microbes	Genes	Primer sequence	nMoles
MDR *E. coli.*	*acrA*-F	5'- CTCTCAGGCAGCTTAGCCCTAA -3'	39.4
	acrA-R	5'- TGCAGAGGTTCAGTTTTGACTTT -3'	35.0
	acrB-F	5'- AAGAAGCTACCCGTAAGTCG -3'	25.9
	acrB-R	5'- AGTAGAACCGCCAAAGAAGG -3'	30.3
MDR *P. aeruginosa*	*MexA*-F	5'- ACCTACGAGGCCGACTACCAGA -3'	33.7
	MexA-R	5'- GTTGGTCACCAGGGCGCCTTC -3'	31.5
	MexB-F	5'- GTGTTCGGCTCGCAGTACTC -3'	35.6
	MexB-R	5'- AACCGTCGGGATTGACCTTG -3'	41.3
MDR *S. aureus*	*norA*-F	5'- TGTTAAGTCTTGGTCATCTGCA -3'	31.3
	norA-R	5'- CCATAAATCCACCAATCCC -3'	25.4
	norB-F	5'- ATGGAAAAGCCGTCAAGAGA -3'	26.2
	norB-R	5'- AACCAATGATTGTGCAAATAGC -3'	33.6
MDR *Candida albicans*	*ERG11*-F	5'- ACCCTGAAGATTTTGATCCAACTAGATG-3'	24.3
	ERG11-R	5'- CCCAAACCCATAATCAACTTCATCAGA -3'	23.0
	TAC1-F	5' - TGGCAATGTATTTAGCAGATGAGG -3'	16.5
	TAC1-R	5' - TGCTTGAACTGAGGTGAATTTTG -3'	19.9
Housekeeping gene	*ampC-F*	5'- GGTGCAGAAGGACCAGGCACAGAT-3'	31.2
	ampC-R	5'- CGATGCTCGGGTTGGAATAGAGGC-3'	35.6

4.2.2.9. Hemolysis test

The assessment of the hemolytic capacity is crucial in order to guarantee the safety of nanoparticles when applied to wounds, distilled water, saline, Au-NPs, Au-TMC-NPs, Ag-NPs, Ag-TMC-NPs and Au-Ag-TMC-NPs were used for the comparison. Human blood was drawn from healthy volunteers, and plasma was separated by centrifugation, followed by three PBS washes. Concisely 200 µL of washed blood was added along with 800 µL of each nanoparticle sample [144]. Follwed by incubation of all tubes for 2 h at 37°C then centrifuged at 3000 rpm for 8 min. was done, and 100 µL of the supernatant was then subjected to 96-well plates and the absorbance was recorded at 540 nm. The percentages of hemolysis were computed using the equation 1:

$$\%\ Hemolysis = \frac{Optical\ density\ of\ test - Optical\ density\ of\ PBS}{Optical\ density\ of\ distilled\ water - Optical\ density\ of\ PBS} X\ 100 \quad (1)$$

4.2.3. Preparation and characterization of Au-Ag-TMC-NPs-NFs nanofibers

A 4% solution (w/v) of Chitosan (CS) was prepared by dissolving it in a binary solvent system consisting of acetic acid and distilled water (80/20 ratio) at a temperature of 80°C, using magnetic stirring. Polyvinyl alcohol (PVA) solutions with a weight concentration of 5% were generated by disintegrating PVA powder in distilled water in controlled conditions, ensuring a constant temperature of 70°C. The chitosan 4 wt.%-PVA 5 wt.% solution was prepared by combining CS and PVA solutions in a 1:1 volume ratio [145]. When chitosan 4 wt.% and PVA 5 wt.% solutions are combined in a 1:1 volume ratio, the resulting final concentrations are halved to 2 wt.% chitosan and 2.5 wt.% PVA, respectively. Further, Au-Ag-TMC-NPs solution (1 mL) was introduced to CS-PVA solution (2.5 mL). The CS-PVA-Au-Ag-TMC-NPs mixture was subjected to intense stirring for 2 h. The uniform gel obtained was used for the processes of drop-casting or electrospinning.

4.2.3.1. Electrospinning process

During a conventional electrospinning procedure, a mixture containing CS-PVA-Au-Ag-TMC-NPs was introduced into a syringe pump and subjected to electrospinning under a positive voltage of 15 kV. The distance between the target and the tip of the needle used for collection was 12 cm. The collection plate used in the experiment was a grounded aluminium foil. The flow rate was consistently maintained at 0.4 mL/h, the rotating drum speed was set at 5000 rpm, and the electrospinning process was conducted for a duration of 3h (**Figure 4.3.)** [146].

Au-Ag-TMC-NPs

↓

4% (w/v) Chitosan + 9 % PVA aqueous solution + 1 % Formic acid viscous solution

↓

Mixed on magnetic stirrer for 3 hr

↓

Filled into a syringe

↓

Electrospinning

Voltage=14 Kv
Distance= 12 cm
Flow rate= 0.5 ml/hr
Spinning time= 4 hr
RPM= 5000 RPM

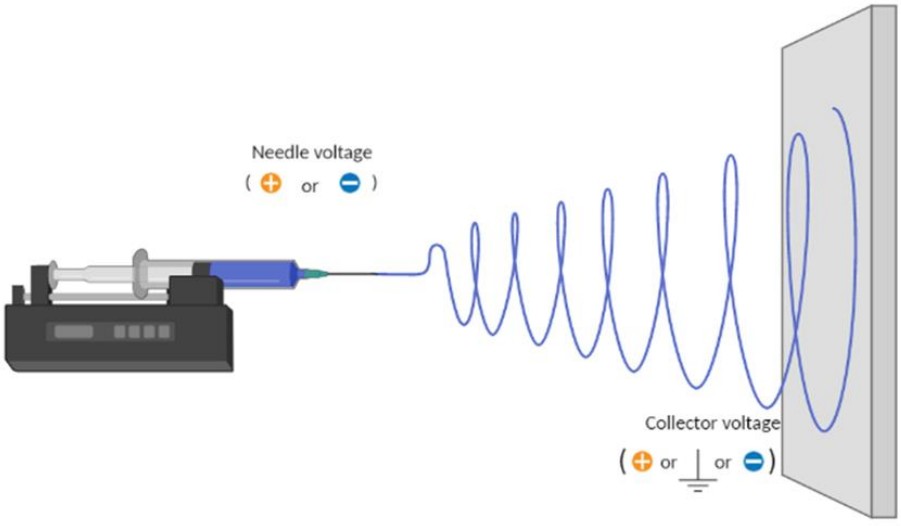

Figure 4.3. Electrospinning processing flow chart and parameters

4.2.3.2. Contact angle measurement

The water contact angle analyzed by using an instrument First-Ten-Angstroms, Portsmouth, VA, USA was used. Electrospun nanofibers membrane samples (1 cm x 1 cm) were removed and introduced on a testing plate, and then distilled water was poured onto the surfaces of the membranes [147]. Camera measurements were used to compare the contact angles of blank nanofibers with those of Au-Ag-TMC-NPs-NFs.

4.2.3.3. FT-IR analysis

The FT-IR technology was used to investigate the various functional moieties present in the electrospun nanofibers by using Nicolet iS5 of THERMO Electron Scientific Instruments LLC within the range of 4000–500 cm^{-1} wavenumber.

4.2.3.4. XRD analysis

The XRD examination of electrospun nanofibers were conducted utilising a Bench Top X-Ray Diffraction instrument. (BT-XRD: RIGAKU Corporation).

4.2.3.5. TEM analysis

Nanofibers spun in a coaxial direction were spread out on a copper TEM grid for a field emission TEM analysis (Tecnai G2 20 TWIN).

4.2.3.6. SEM analysis

The examination of the morphology of nanofibers was conducted using a field emission SEM subsequent to the application of carbon sputtering (model EVO-Scanning Electron Microscope MA15/18, Carl Zeiss Microscopy Ltd.)

4.2.3.7. AFM analysis

Topography and morphology of electrospun nanofibers were analyzed using NTEGRA Prima of NT-MDT Service & Logistics Ltd. (SNL/10, silicon tip with nitride lever). Droplets of the aqueous nanofiber solution were vacuum dried on mica for 8h before being scanned in Scan-Asyst-peak force tapping style in an ambient air environment. AFM utilizes a scanning mechanism equipped with a Silicon (Si) cantilever that is positioned

vertically adjacent to the sample. The resonant frequency of the cantilever, which represents its natural oscillation frequency when not influenced by external forces, is employed as the driving frequency for the scanning process.

4.2.3.8. Water retention capacity

By immersing the nanofibers in a PBS solution (pH 7.4) for 48 h at 37°C, we determined the nanofibers' ability to hold water. The samples were taken out of the solution at predetermined intervals, blotted dry using tissue paper, and then weighed on the precision electronic weighing scale. Triplicates of each samples were tested. The percentage of water retention was calculated using equation 2:

$$Water\ retention\ (\%) = \left(\frac{Wwet - Wdry}{Wdry}\right) X\ 100 \qquad (2)$$

Where, W_{dry} and W_{wet} are the dry and wet sample weights, respectively, before and after being submerged in the PBS solution.

4.2.3.9. Nanofiber stability and degradation

The investigation focused on the stability and deterioration of the nanofibers via the process of immersing the samples in the PBS (pH 7.4) and lysozyme solution (105 U/mL in water) at 37°C. Degradation of lysozyme was monitored for up to 20 days, during which time the lysozyme solution was replaced every 3 days. At the 10^{th} and 20^{th} day, Subsequently, specimens were extracted from the solution and subjected to two rounds of rinsing with distilled water [148]. The equation 3 used to determine the percentage of deterioration is as follows:

$$Degradation\ (\%) = \left(\frac{Wi - Wf}{Wi}\right)\ X\ 100 \qquad (3)$$

Where, the W_i and W_f were pre-degradation and post-degradation sample weights, respectively.

4.2.3.10. Thermal stability

Thermogravimetric analysis was performed on electrospun nanofibers via TGA-50 model of M/s Shimadzu (Asia-Pacific) Pte Ltd. The experiments were conducted at heating rates of 10°C/min, ranging from an initial temperature of 30°C to a final temperature of 700°C.

4.2.3.11. *In vitro* release study

The dialysis bag diffusion technique was used to assess the release profile of Ag^+ and Au from the produced Au-Ag-TMC-NPs and Au-Ag-TMC-NPs-NFs. In a concise manner, a volume of 1 ml of Au-Ag-TMC-NPs was placed into a dialysis bag with a molecular weight cutoff of 1 kD and thereafter sealed in an airtight manner. On the other hand, Au-Ag-TMC-NPs-NFs was cut into smaller pieces (1cm x 1cm), approximately 10 mg of the sample were submerged in 1 ml of PBS (pH 7.4) at a temperature of 37°C. The sample was then placed into a dialysis bag with a molecular weight cutoff of 1 kD and securely sealed. The dialysis bag was submerged in a glass flask containing 100 mL of PBS medium (pH 7.4). The whole experimental apparatus was positioned inside a water-bath shaker (Remi CM-12 Plus, Vasai) set at a temperature of 37 ± 0.5°C, while maintaining a constant shaking motion [149]. According to the pre-established time-intervals of 1 h, 2 h, 3 h, 6 h, 8 h, 12 h, 24 h, and 48h, 1 mL samples were collected and an equivalent amount of fresh medium was added. Subsequently, the samples underwent analysis by UV-visible spectroscopy at a 517 nm wavelength. The concentration of the unknown material was determined by employing a pre-established standard calibration curve ($R2 = 0.9902$) specific to the Au-Ag bimetallic complex.

4.2.3.12. Hemolysis study of nanofibers

Nanofibers were put through a hemolysis test to see if they were safe for human use. The ability of red blood cells (erythrocytes) to break down and release haemoglobin into plasma was measured in this assay. However, erythrocytes represent a highly relevant and well-established model for initial biocompatibility and cytotoxicity screening due to their

abundance in circulation, sensitivity to oxidative stress, and ability to reflect membrane integrity and hemolytic effects critical for systemic safety evaluation. Furthermore, erythrocytes undergo eryptosis, a form of programmed cell death analogous to apoptosis in nucleated cells, providing valuable insight into cytotoxic mechanisms. Given resource constraints and the comprehensive nature of the erythrocyte assays conducted through hemolysis study which sufficiently demonstrate the biocompatibility profile of the nanofibers. Dressings are divided into three categories based on their index of hemolysis, as defined by ASTM F 756-00 (2000) [150]: (1) The use of a hemolytic dressing, resulting in a hemolysis rate above 5%, (2) The dressing has a modest hemolytic effect, characterized by a hemolysis rate ranging from 2% to 5%; and (3) The dressing under consideration is non-hemolytic, as shown by its hemolytic index of 2% [151]. The hemolysis produced by Au-Ag-TMC-NPs-NFs was compared with distilled water, saline and Au-Ag-TMC-NPs on healthy erythrocytes.

4.2.3.13. Whole blood clotting ability

In order to assess the hemostatic properties of the nanofibers, the nanofiber film was placed separately in glass petri dishes and preheated to a temperature of 37°C [152]. Subsequently, 200 µL of fresh human blood was applied onto the surface of each film, and an additional 30 µL of 0.2 M $CaCl_2$ solution was introduced to commence the process of coagulation. The petri-plates holding the nanofibers were then incubated at 37°C for 10 min. Followed by 10 min incubation period, 30 mL of distilled water was carefully introduced drop by drop to all petri-plates avoiding disrupting the clot. This procedure was conducted in order to facilitate the hemolysis of red blood cells that were not entrapped inside the clot, using a volume of 25 mL of water. Following this, the measurement of absorbance was conducted on the resultant solution of haemoglobin at a specific wavelength of 540 nm.

4.2.3.14. Thrombus development analysis

Gravimetric analysis was utilized to investigate thrombus development on nanofibers [153]. In the usual procedure, the nanofiber film (1×1cm), was immersed in a solution of saline for a duration of 24h at a temperature of 37°C. Followed by the extraction of nanofiber from solution of saline and then exposed to 1.5 mL of acid citrate dextrose blood, which was carefully applied onto the surface of the nanofibers. Followed by the introduction of 20µL of a 0.2 M calcium chloride solution to induce the development of a thrombus within a time frame of around 3-4 min. The process of thrombus development was halted by the introduction of 8 ml distilled water at the mark of 20 min. Clot was then immersed in a 40% solution of formalin (10 ml) for a duration of 10 min. Ultimately, the immobilized clot was rinsed with water, gently dried with soaking paper, and afterwards weight measure.

4.2.4. *In vivo* study of Au-Ag-TMC-NPs-NFs distribution on wound site

In vivo fluorescence optical imaging of blank nanofiber with free-DiD (control), Au-Ag-TMC-NPs-NFs-DiD was performed on uninfected and different microbial infected wounds in mice utilizing the Photon-Imager-Optima-System (Biospace Lab). The free-DiD and DiD tagged Au-Ag-TMC-NPs-NFs equivalent to 200nM of DiD dye were applied to the wound, The fluorescence signals were recorded at excitation and emission wavelengths of 620 and 710 nm, respectively, after 10 min. At time intervals of 2, 4, 8, 24, and 48h after the application. The analysis of radiant efficiency quantified as the ratio of fluorescence intensity to the product of area and time, was conducted using the imaging software provided by Biospace Lab. This analysis included using the region of interest (ROI) tool to surround the specific area of the wound.

4.2.5. Wound healing study

4.2.5.1. *In vivo* wound healing study

A wound healing potential study was performed in mice (Swiss albino, 18-22 g weight). The Institutional Animal Ethics Committee (IAEC) at the Indian Institute of Technology (Banaras Hindu University), Varanasi, UP, India, approved all *in vivo* animal experiments (IAEC Approval Number: IIT(BHU)/IAEC/2023/041) and the studies were carried out in compliance with the guidelines provided by the National Research Council's Guide for the Care and Use of Laboratory Animals. The animals were housed in controlled environments where temperature was regulated, humidity levels were maintained at a regular level, and a 12h light/dark cycle was implemented. The mice (n=5) were randomly assigned to seven different groups. The excision wound mice model was established by applying hair removal lotion to the dorsal region, followed by shaving. A circular region with an estimated size of about 314 mm^2 was generated subsequent to the administration of ketamine (50 mg/kg, body weight- i.p.) to anaesthetize the animals [122]. The wound of each of the seven mice groups was deliberately infected by introducing the corresponding MDR microorganisms onto the location of the lesion. In this study, a commercial formulation of ciprofloxacin ointment, which is a broad-spectrum antibiotic, was used as the positive-control. Conversely, the negative-control consisted of an untreated lesion. One cohort is maintained in a non-infected state and is undergoing treatment with the Au-Ag-TMC-NPs-NFs. Furthermore, several demographic cohorts are experiencing infections caused by distinct MDR microbial strains. The grouping of the experimental mice was as follows:

The experimental groups

Group I: The wounds of the mice were left untreated;

Group II: The wounds of the mice were with marketed application of ciprofloxacin ointment USP of 0.3% (w/w); a concentration;

Group III: The wounds of the mice were keep uninfected and treated with the use of Au-Ag-TMC-NPs-NFs therapy (3.25 μg ml^{-1});

Group IV: The wounds of the mice were infected by the process of inoculation with the MDR *E. coli.* bacteria on the wound sites followed by the treatment with Au-Ag-TMC-NPs-NFs (0.390 μg ml^{-1});

Group V: The wounds of the mice were infected by the process of inoculation with the MDR *Pseudomonas aeruginosa* bacteria on the wound sites followed by the treatment with Au-Ag-TMC-NPs-NFs (0.781 μg ml^{-1});

Group VI: The wounds of the mice were infected by the process of inoculation with the MDR *S. aureus* bacteria on the wound sites followed by the treatment with Au-Ag-TMC-NPs-NFs (0.195 μg ml^{-1});

Group VII: The wounds of the mice were infected by the process of inoculation with the MDR *Candida albicans* bacteria on the wound sites followed by the treatment with Au-Ag-TMC-NPs-NFs (3.125 μg ml^{-1});

Treatment was delivered once a day from the beginning of the operation to the end of the recovery period. The software tool ImageJ was used to quantitatively assess the extent of wound healing over a period of time by the comparison of area of wound at a certain period with the initial area of wound. The relative percent area of the wound was plotted against time in order to get an understanding of the rate at which it was recovering.

4.2.5.2. Histopathological studies

Following a period of 12 days, the mice in each respective groups were died using CO_2 asphyxia. Subsequently, their layer of skin with wounds was carefully removed, and the resulting tissues were preserved in a solution of formalin with a concentration of 10% v/v. Additionally, a rotary microtome was used to cut 10 μm thick slices of paraffin-embedded tissue. Staining with hematoxylin and eosin was employed to examine the tissue slices. A

bright field microscope (Dewinter microscope) and Capture pro 4.1 software were used to observe the histological changes under the microscope [154] .

4.2.6. *In vivo* ultrasound/photoacoustic study

The wound model of mice was made after infection of the wound with MDR microbes was used for *in vivo* photoacoustic study. Then mice were divided into groups of seven, with each group consisting of three mice (n = 3). After that, all the animals were scanned under an ultrasound /photoacoustic imaging system (Vevo LAZR_X Vevo 3100, Toronto, Canada, 40 MHz ultrasound array transducer). The wound was scanned in B mode of ultrasound, for the vascularity study the power Doppler mode was on whereas for oxygenated/deoxygenated blood the photoacoustic mode was on. Photoacoustic/ultrasound imaging of the wound was visualized on 1^{st}, 4^{th}, 8^{th}, and 12^{th} day post-treatment. The ultrasound/photoacoustic pictures were superimposed in order to ascertain the dimensions and oxygen saturation of the wound. Power Doppler image setting was done to analyzed wound vascularity. For the processing of images, the Vevo-LAB-software (FUZIFILM Visual Sonics, Toronto, Canada) was used [155].

4.2.7. Western blot study of wound marker protein

The western blot method was used to illustrate the manifestation of the wound healing marker proteins like the vimentin mesenchymal marker associated with epithelial-mesenchymal transition (EMT), SMAD2, and phospho MAPK (ERK 1/2) [154]. Wound skin tissues of untreated mice, and mice treated with marketed formulation, uninfected mice treated with Au-Ag-TMC-NPs-NFs, and microbial infected mice (MDR strains of *E. coli.*, *P. aeruginosa*, *S. aureus*, and *C. albicans*) treated with Au-Ag-TMC-NPs-NFs were dissected on ice. Approximately 5.0 mg of tissue was homogenized in 300µl of ice-cold 1X RIPA lysis buffer (50mM Tris–HCl pH 7.4, 1% NP-40, 0.25% sodium-deoxycholate, 150 mM NaCl, 1mM EDTA) using electric homogenize [156]. Protein concentration was

measured by nanodrop (Thermo Scientific) and samples containing ~70 µg of protein were denatured and run at 12% SDS-PAGE gel. Separation of the peptides on SDS-PAGE was followed by overnight transfer of proteins from the gel onto a PVDF membrane. Following the application of a 4% skimmed milk solution in TBST, the blocking process was conducted, the membrane was incubated with primary antibody followed by AP-conjugated secondary antibody. Chromogenic detection of the signal was carried out using Sigma FAST NBT/BCIP. The primary antibodies used for western blotting were Rabbit anti-Vimentin (1:1000), Rabbit anti-Phospho SMAD2 (1:1000), Rabbit anti-Phospho MAPK (ERK 1/2) (1:2000), Rabbit anti-β Actin (1:1000). Expression of Vimentin was significantly increased in protein samples obtained from mice infected with MDR *P. aeruginosa* and treated with Au-Ag-TMC-NPs-NFs, in comparison to a control group of untreated animals. ImageJ was used for the analysis of the intensity of the protein bands.

4.2.8. Statistical analysis

All the *in vivo* and *in vitro* data were interpreted by using Graph Pad Prism 9.0 software. All the data was triplicated and presented as mean ±SD. Statistical significance among groups was calculated by One-Way ANOVA and t-test. The values ns ($p \geq 0.05$), * ($p < 0.05$), ** ($p < 0.01$), *** ($p < 0.001$), and **** ($p < 0.0001$) were considered for significance level determination.

4.3. Results

4.3.1. Characterization of nanoparticles

4.3.1.1. Particle size, PDI and surface charge

The particle size, PDI and surface charge of synthesized nanoparticles were found to be in the range of 82.6 ± 4.8 nm to 133.7± 9.5 nm, 0.106 ± 0.082 to 0.239 ±0.062 and 18.4 ± 2.5 mV to 54.4 ± 1.8 mV respectively (**Table 4.3. and Figure 4.4.**). Results revealed that uniformly dispersed Au-Ag-TMC-NPs possess a higher positive charge than their

monometallic and bimetallic counterparts. Whereas all the TMC-based nanoparticle surfaces had charges between +45 and +54 mV, demonstrating their high level of stability due to TMC [88].

4.3.1.2. UV/Vis spectroscopy

The comparative UV–vis spectra of the synthesized nanoparticles are depicted in **(Figure 4.5.)**. UV–vis spectra were observed in the range from 535 to 480 nm [157].

Table 4.3. PS, PDI and zeta potential of the synthesized nanoparticles

Nano-formulation	Particle Size (nm) (Mean ± SD)	Polydispersity index (Mean ± SD)	Zeta potential (mV) (Mean ± SD)
Au-NPs	64.99 ± 3.0	0.131 ±0.073	21.6 ± 1.5
Au-TMC-NPs	125.6 ± 4.8	0.190 ±0.097	42.1 ± 2.8
Ag-NPs	118.1 ± 5.1	0.239 ±0.062	18.4 ± 2.5
Ag-TMC-NPs	133.7± 9.5	0.106 ± 0.082	45.9 ± 2.0
Au-Ag-NPs	80.30 ± 5.4	0.170 ± 0.069	20.3 ± 1.4
Au-Ag-TMC-NPs	108.3 ± 8.4	0.235 ± 0.015	54.4 ± 1.8

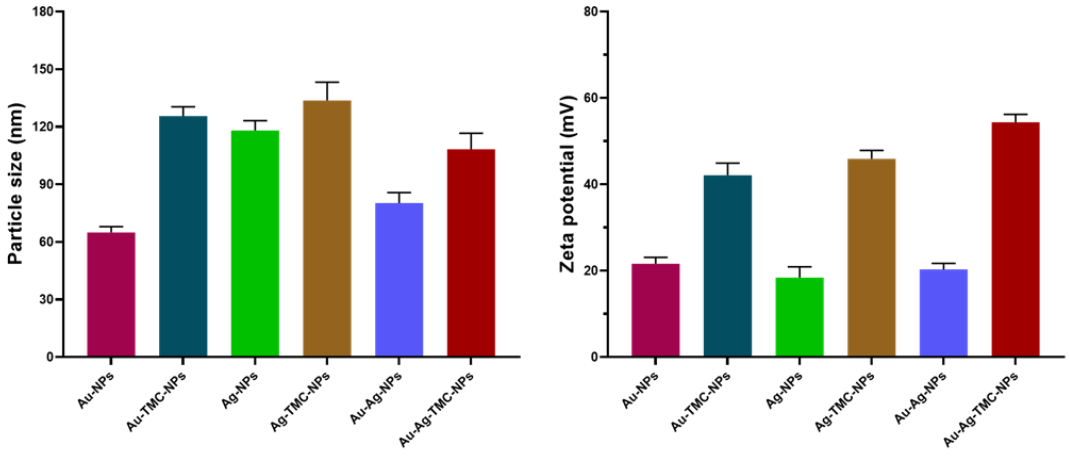

Figure 4.4. Bar diagram for particle-size and zeta-potential of the optimized nano-formulation

4.3.1.3. Transmission electron microscopy analysis

The TEM images of various synthesized nanoparticle formulations were observed at the resolution of 50 nm to 200 nm. The TEM images of Au-NPs, Ag-NPs and Au-Ag-NPs depict a clear and spherical geometry without any outer layer on the surface, whereas Au-Ag-NPs and Au-Ag-TMC-NPs reveal that deposition on the surface of the nanoparticles that could be interpreted as covering of TMC **(Figure 4.6.A)**. The physical nature of all the nanoparticle formulations were examined by TEM-SAED **(Figure 4.6.B)**.

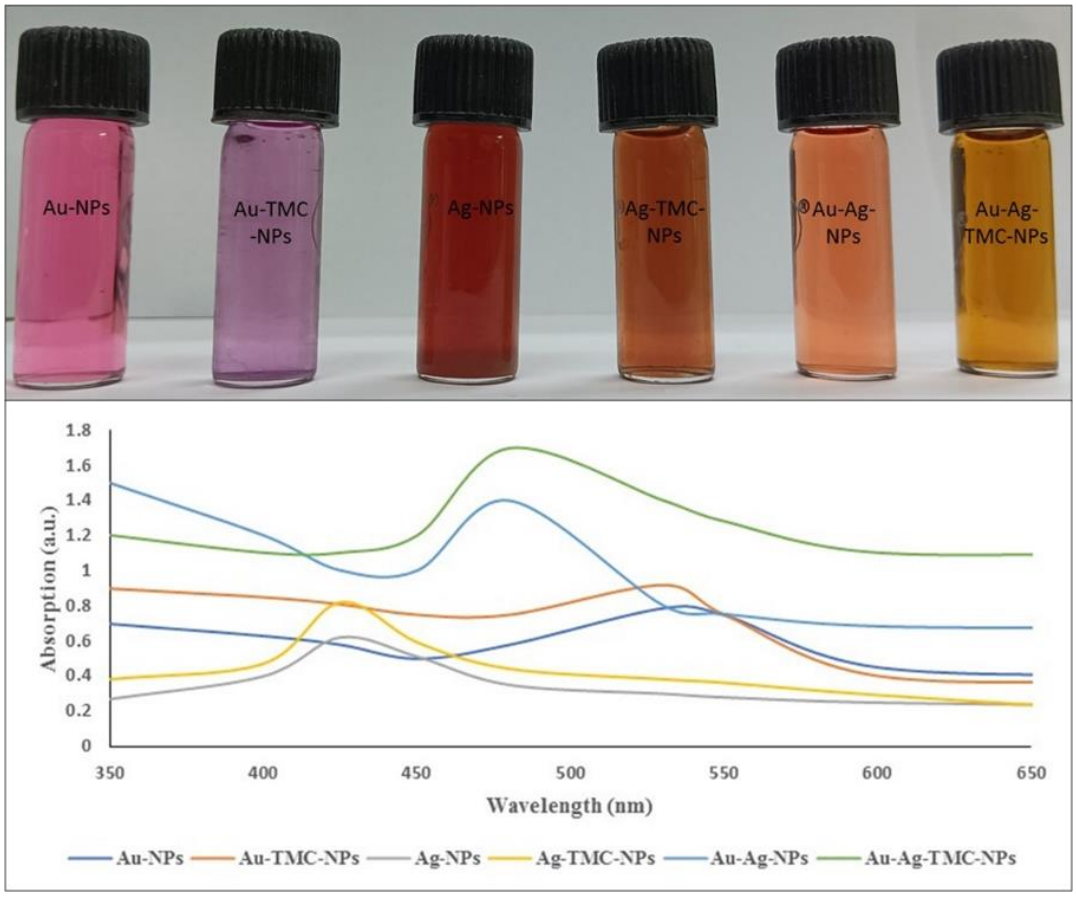

Figure 4.5. UV–Vis absorbance spectra and photographs of synthesized nanoparticle

The SAED image of Au-NPs, Ag-NPs depicts a regular pattern of bright spots, demonstrating its crystalline nature, whereas the SAED images of Ag-TMC-NPs, Au-Ag-NPs and Au-Ag-TMC-NPs formulation showed discrete rings and the spots with an irregular pattern which reveals their polycrystalline nature.

4.3.1.4. Atomic force microscopy analysis

The surface topography of the synthesized nanoparticle formulations was analyzed by the AFM, as demonstrated in **(Figure 4.6.C, D)** nanoparticles are round, smooth, and devoid of visible pinholes or fissures.

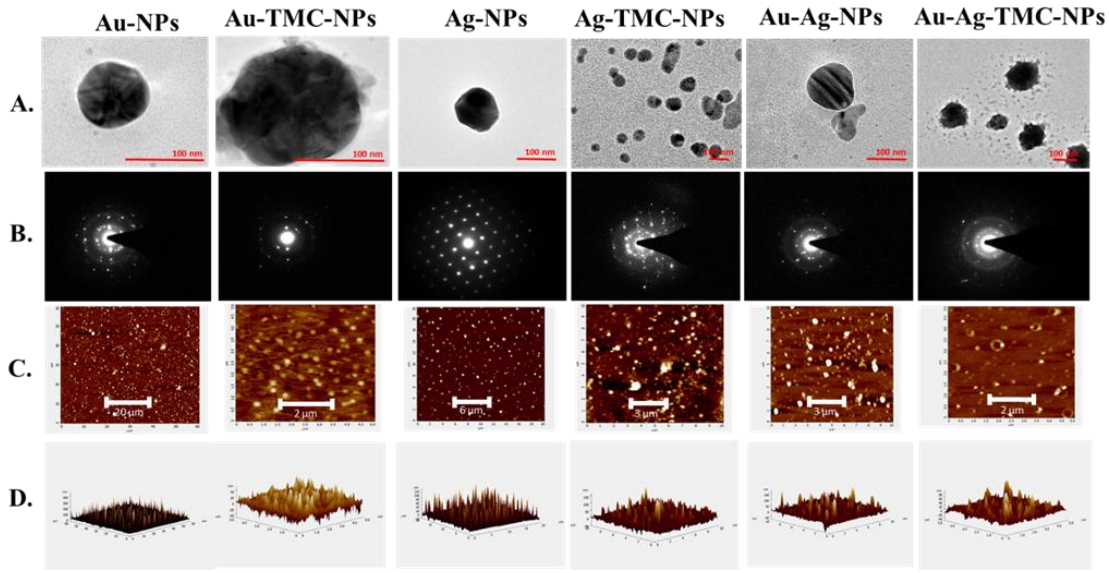

Figure 4.6. (A) TEM, (B) SAED, (C) 2D AFM, (D) 3D AFM of synthesized nanoparticle formulations

4.3.1.5. STEM-EDX analysis

The Au-Ag-TMC-NPs were subjected to elemental analysis by STEM-EDX analysis, which conclusively verifies the existence of gold and silver metals. **Figure 4.7.** illustrates a graphical depiction of the atomic proportion of Ag and Au is 85.59% and 14.41% respectively.

4.3.2. Antimicrobial activity of nanoparticles

4.3.2.1. MIC, MBC and MFC

According to the MIC, MBC and MFC, the potential nanoformulation Au-Ag-TMC-NPs was found to be most effective among all the formulations, including marketed formulation for all the MDR microbial strains, by considering this, all the related studies will be carried

out. For, Au-Ag-TMC-NPs, the ratio of MBC to MIC for MDR *E. coli.* was found to 0.390 μg ml^{-1}/0.390 μg ml^{-1} ⩽1, whereas for MDR *P. aeruginosa* it was 0.781 μg ml^{-1} /0.781 μg ml^{-1} ⩽1, whereas for MDR *S. aureus* it was 0.195 μg ml^{-1} /0.390 μg ml^{-1} ⩽2, and for MDR *C. albicans* it was 3.125 μg ml^{-1} /3.125 μg ml^{-1} ⩽1 **(Table 4.4.) (Figure 4.8.)**.

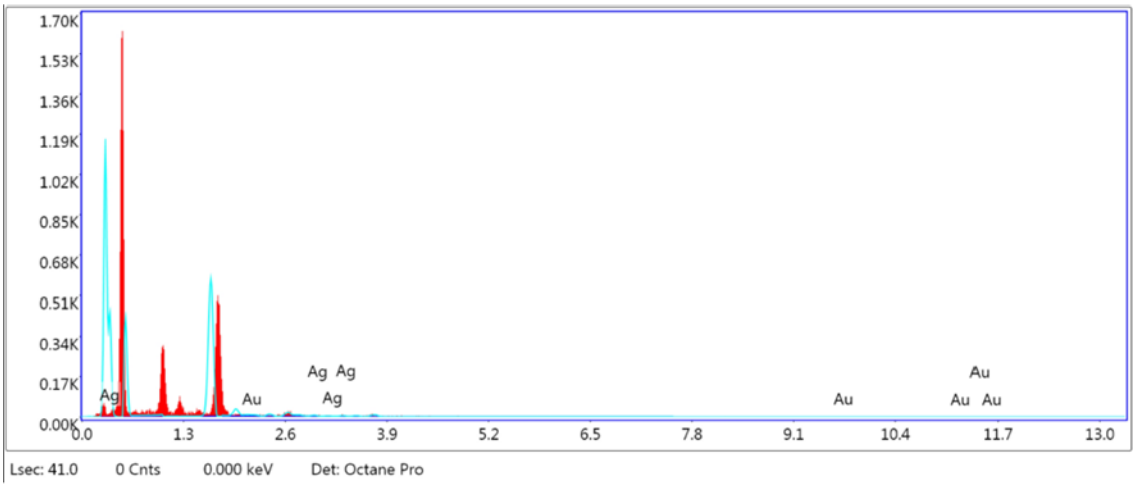

eZAF Smart Quant Results

Element	Weight %	Atomic %	Net Int.	Error %	Kratio	Z	A	F
AgL	85.59	91.56	1.00	30.46	0.7895	1.0192	0.9049	1.0001
AuL	14.41	8.44	0.00	89.83	0.1235	0.8440	1.0076	1.0079

Figure 4.7. Elemental analysis of Au-Ag-TMC-NPs

The MBC to MIC ratio is ⩽4 indicate more potent antibacterial agents. This study demonstrates that the developed nanoformulation Au-Ag-TMC-NPs has superior antibacterial efficacy compared to other nanoformulations. Specifically, it shows significant promise in combating MDR of *S. aureus* and MDR *E. coli.* of MDR *P. aeruginosa* and MDR *C. albicans*.

4.3.2.2. Bacterial susceptibility

The results obtained from the study demonstrated that Au-Ag-TMC-NPs showed maximum zone of inhibition among all other nanoformulations and antibiotic ciprofloxacin **(Table 4.4.).** This experiment revealed that increasing the level of concentration (2-fold approx)

of Au-Ag-TMC-NPs from 0.781 μg ml^{-1} to 1.562 μg ml^{-1} for MDR *P. aeruginosa*, 1.562 μg ml^{-1} to 3.125 μg ml^{-1} for MDR *E. coli.*, 3.125 μg ml^{-1} to 6.25 μg ml^{-1} for MDR *S. aureus*, and 6.25 μg ml^{-1} to 12.5 μg ml^{-1} for MDR *Candida albicans*, the ZOI was slightly increased **(Figure 4.9.)**. This study shoes that the developed nanoformulation Au-Ag-TMC-NPs has great Bacterial susceptibility in comparison to other nanoformulations. Specifically, it shows significant promise in combating MDR of *S. aureus* and MDR *E. coli.* of MDR *P. aeruginosa* and MDR *C. albicans*.

Table 4.4. ZOI of the optimized nanoparticles on MDR *E. coli* and MDR *P. aeruginosa*

	MDR *E. coli.*		**MDR *P. aeruginosa***	
Formulation	MIC ($\mu g\ ml^{-1}$)	ZOI (mm)	MIC ($\mu g\ ml^{-1}$)	ZOI (mm)
Au-NPs	50	1.67 ± 0.21	100	0.70 ± 0.26
Au-TMC-NPs	50	1.73 ± 0.14	100	1.03 ± 0.11
Ag-NPs	12.5	12.02 ± 0.17	25	7.98 ± 0.07
Ag-TMC-NPs	12.5	13.96 ± 0.07	12.5	11.77 ± 0.17
Au-Ag-NPs	1.562	16.27 ± 0.13	3.125	8.27 ± 0.41
Au-Ag-TMC-NPs	0.390	24.93 ± 0.09	0.781	23.56 ± 0.31
Marketed antibiotic	0.781	19.86 ± 0.94	6.25	14.33 ± 0.72

Table 4.5. ZOI of the optimized nanoparticles on MDR *S. aureus* and MDR *C. albicans*

	MDR *S. aureus*		**MDR *Candida albicans***	
Formulation	MIC ($\mu g\ ml^{-1}$)	ZOI (mm)	MIC ($\mu g\ ml^{-1}$)	ZOI (mm)
Au-NPs	50	4.49 ± 0.12	200	No zone
Au-TMC-NPs	25	5.18 ± 0.10	200	No zone
Ag-NPs	12.5	10.66 ± 0.16	100	1.33 ± 0.15
Ag-TMC-NPs	6.25	12.6 ± 0.12	50	1.75 ± 0.08
Au-Ag-NPs	3.125	15.73 ± 0.15	12.5	5.69 ± 0.17
Au-Ag-TMC-NPs	0.195	28.94 ± 0.20	3.125	7.88 ± 0.22
Marketed antibiotic	0.781	20.06 ± 0.53	1.562	10.38 ± 0.20

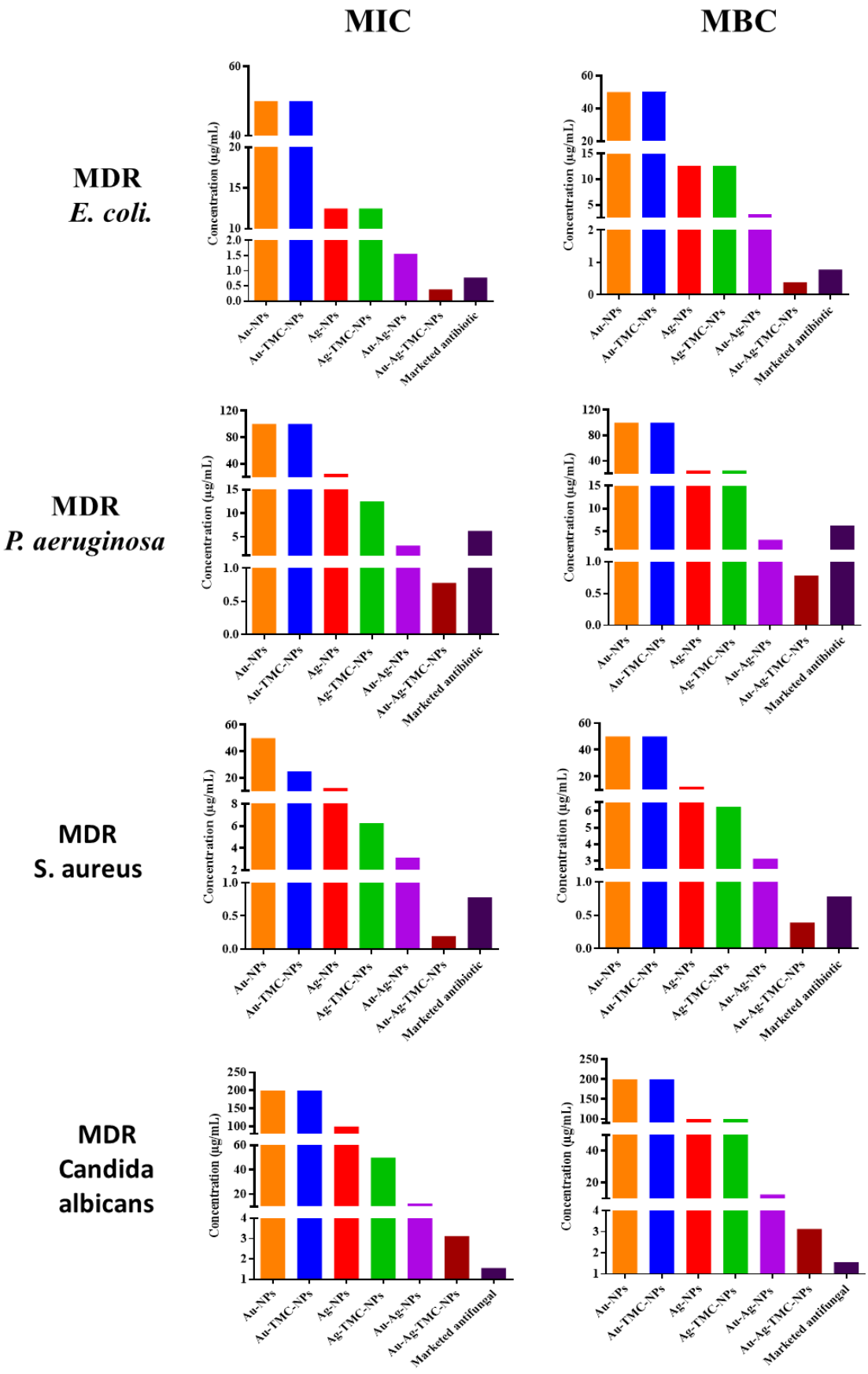

Figure 4.8. The MIC, MBC and MFC of the optimized nanoparticles

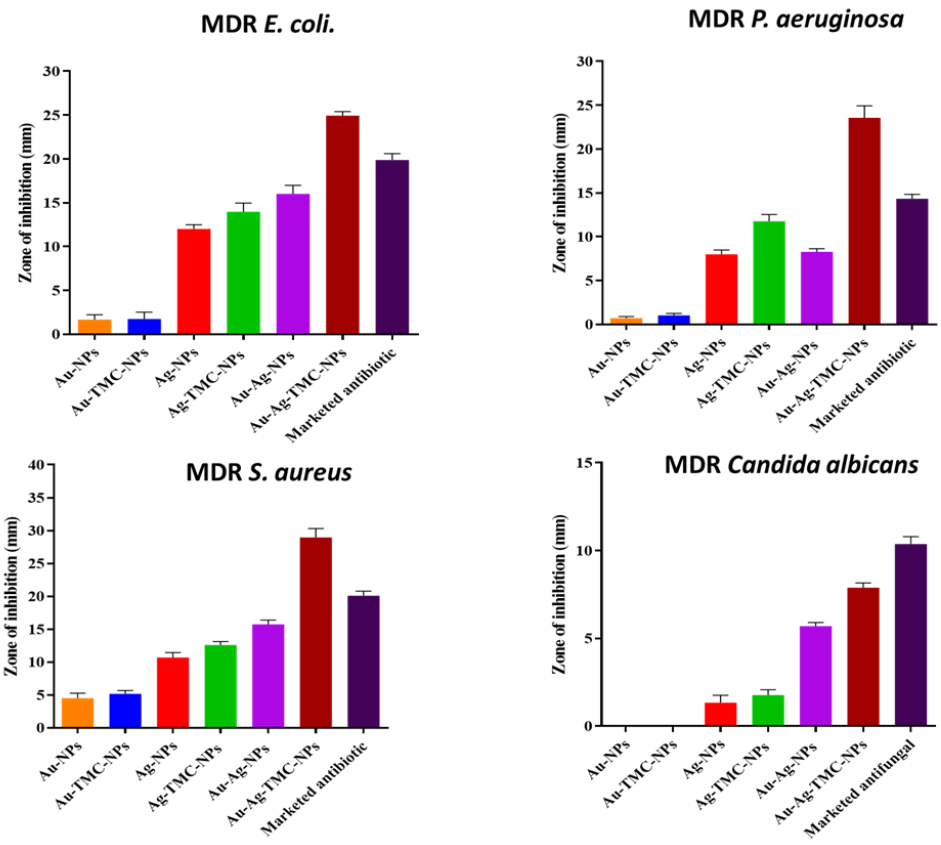

Figure 4.9. Zone of inhibition of the optimized nanoparticles on various MDR microbes

4.3.2.3. Bacterial viability test

The assessment of bacterial viability was assessed by live dead assay, after treatment with Au-Ag-TMC-NPs revealed that initially (0 h), the % of viable cells of MDR *E. coli.* **(Figure 4.10.)** was 52.14 ± 1.56%. However, following a duration of 6 h, and 12 h of treatment, these % decreased significantly to 15.56 ± 0.10% and 3.11 ± 0.11%, respectively. Furthermore, for MDR *P. aeruginosa* **(Figure 4.11.)** the viable cells were 88.03 ± 1.93% in the beginning (0 h), but after 6 h, and 12 h treatment, they were found to be 24.13 ± 0.24% and 0.76 ± 0.01%, respectively. The visible cells for MDR *S. aureus* **(Figure 4.12.)** were 75.54 ± 2.93% in the beginning (0 h), but after 6 h, and 12 h treatment, they were found to be 30.13 ± 1.24% and 5.76 ± 0.84%, respectively. For MDR *C. albicans* **(Figure 4.13.)** the viable cell count was 48.54 ± 2.64% in the beginning (0 h), but after 6 h, and 12 h of

treatment, they were found to be 31.13 ± 1.12% and 8.76 ± 0.47%, respectively. The quantification of living and dead cells in the individual CLSM pictures was performed using Image-J software, as seen in **Figure 4.14.** Due to the increased surface free energy of the surface Ag atoms in the bimetallic NPs structure, Au-Ag core-shell NPs may have enhanced antibacterial characteristics. The Au-Ag-TMC-NPs exhibited a substantial reduction in the count of live cells and concurrent rise in the count of dead cells when interacting with the MDR bacterial strains, demonstrating a strong antibacterial synergy.

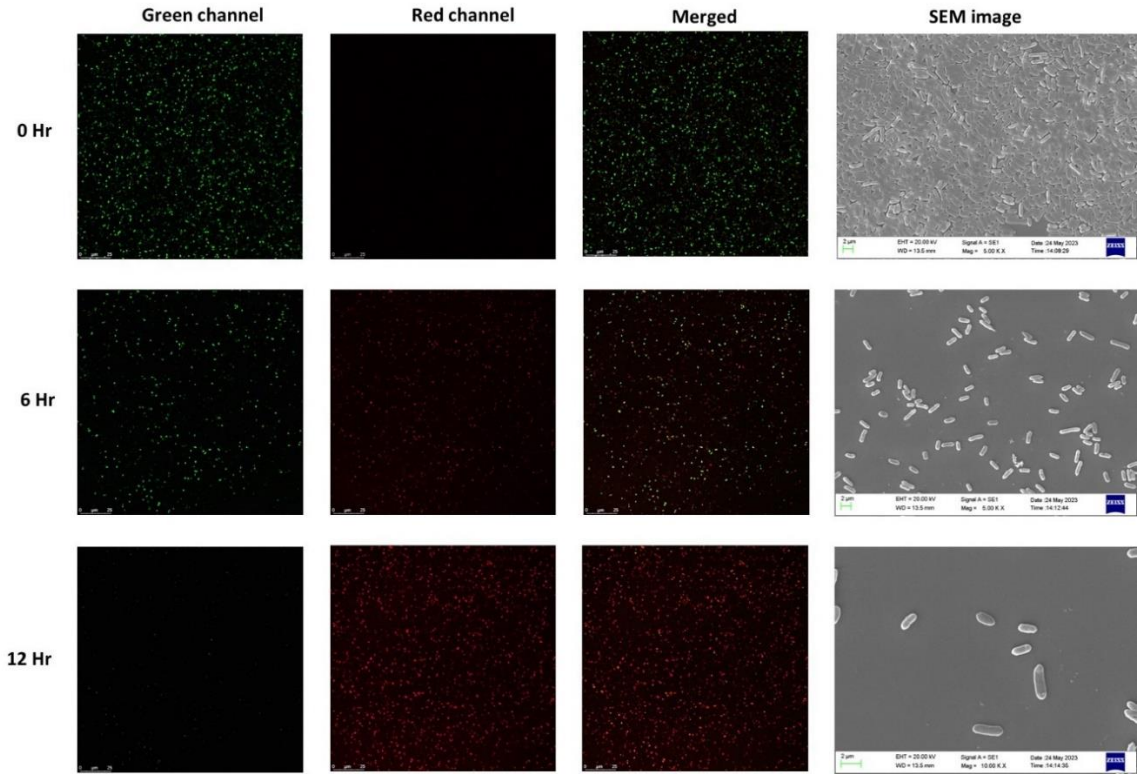

Figure 4.10. CLSM images of MDR *E. coli.* after treatment with Au-Ag-TMC-NPs

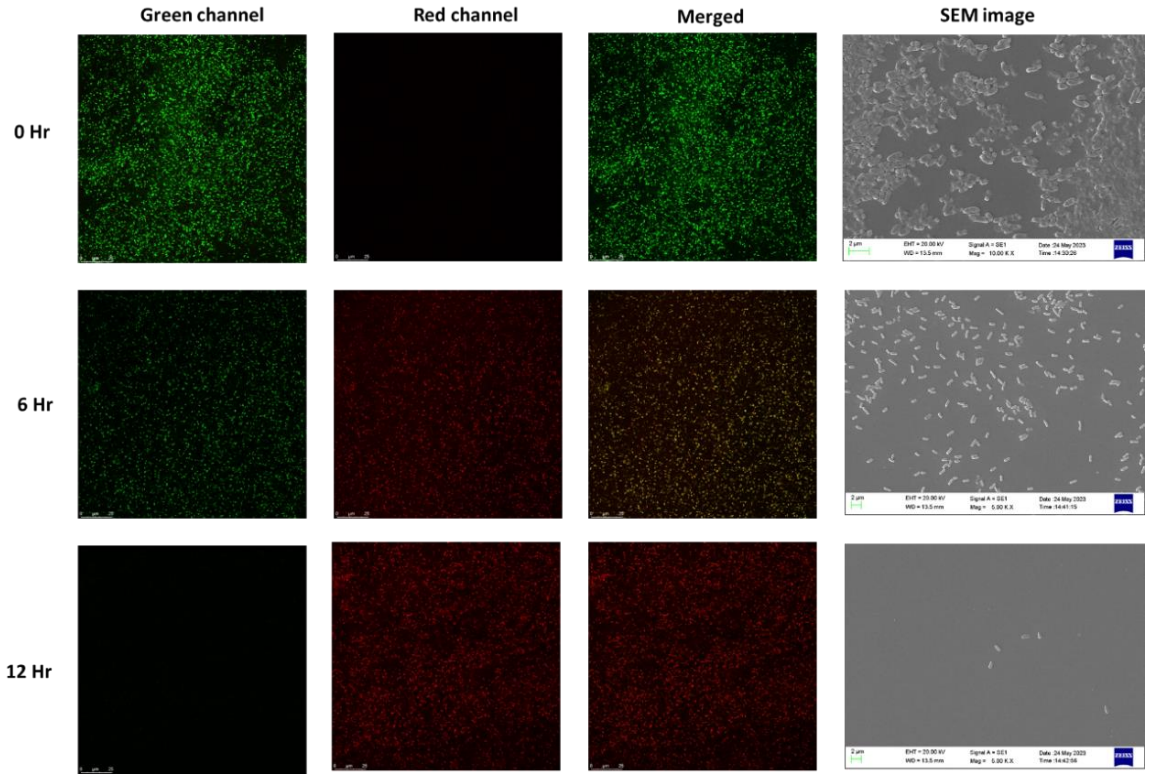

Figure 4.11. CLSM images of MDR *P. aeruginosa* after treatment with Au-Ag-TMC-NPs

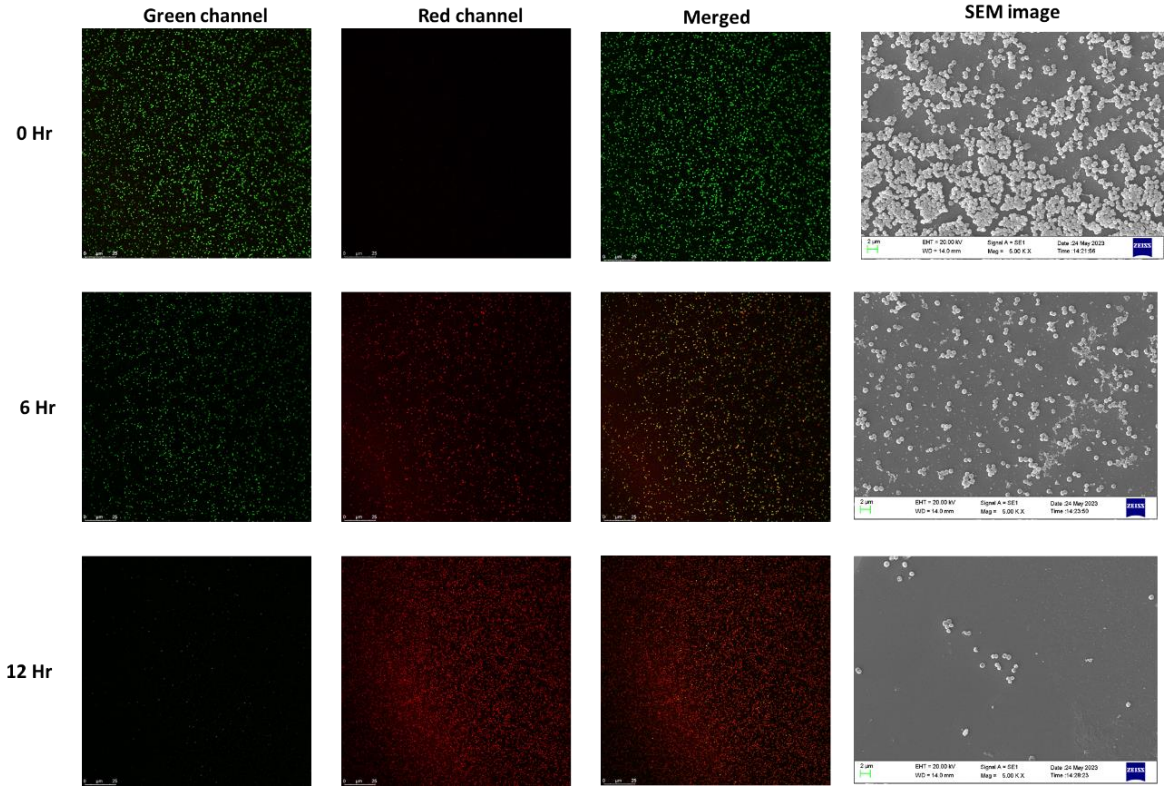

Figure 4.12. CLSM images of MDR *S. aureus* after treatment with Au-Ag-TMC-NPs

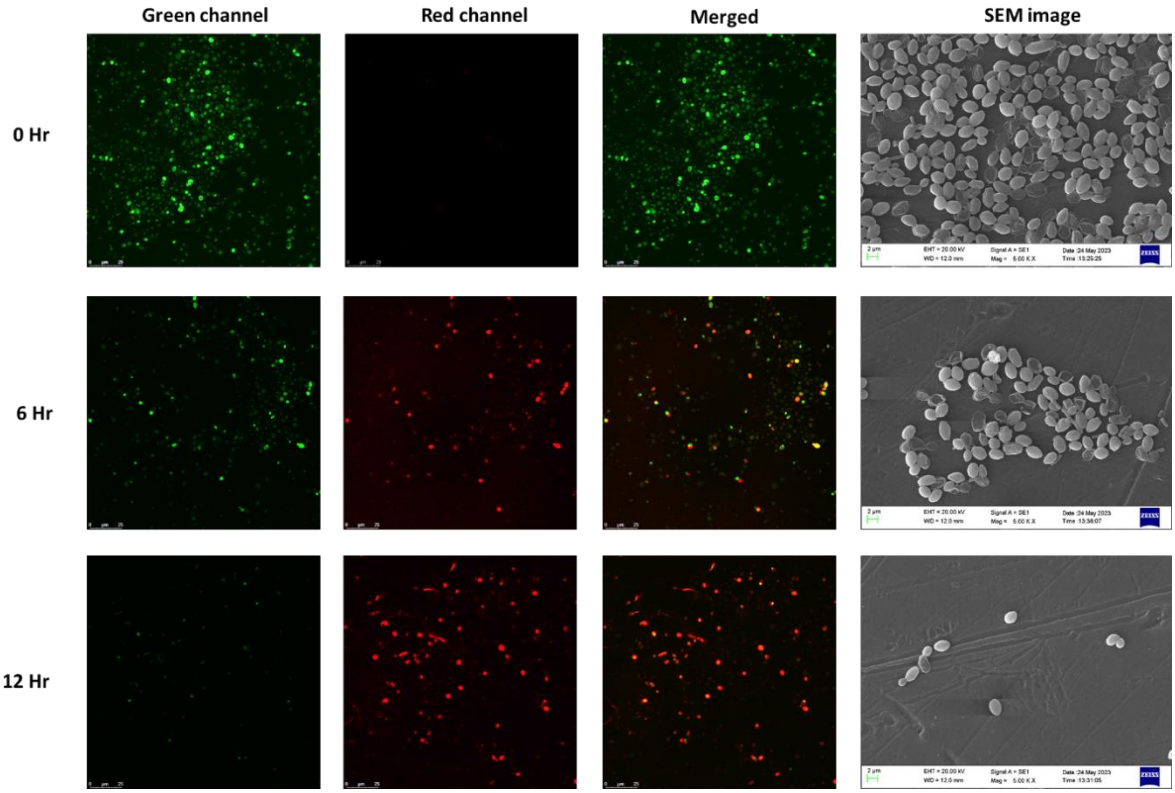

Figure 4.13. CLSM images of MDR *C. albicans* after treatment with Au-Ag-TMC-NPs

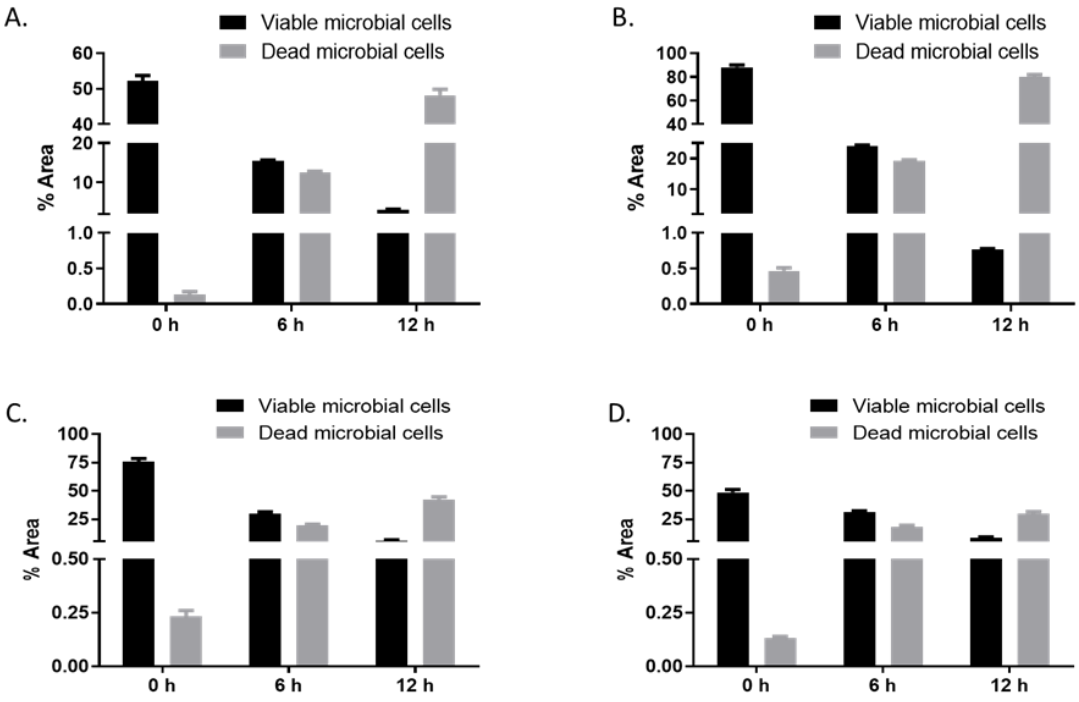

Figure 4.14. Bar diagrams of dead and viable microbial cells count: A) *E. coli.*; B) *P. aeruginosa*; C) *S. aureus*; D) *Candida albicans*

4.3.2.4. Antibiofilm activity

The electron micrograph of the test microorganism after treatment with Au-Ag-TMC-NPs treatment showed the damage of the biofilm over time. The findings of the SEM and AFM analysis provide confirmation that Au-Ag-TMC-NPs exhibit a significant antibiofilm action **(Figure 4.10. to Figure 4.18.)**. The observed phenomenon might perhaps be attributed to the heightened infiltration of Au-Ag-TMC-NPs with positive charges, enhanced binding affinity to the biofilm. The results suggest upon exposure to NPs, a time-dependent decrease in biofilm development was seen in MDR strains. The Au-Ag-TMC-NPs are efficient against multidrug-resistant microbial cells in biofilms and effectively reduce the resistance of stationary bacterial and fungal cells to antimicrobial drugs.

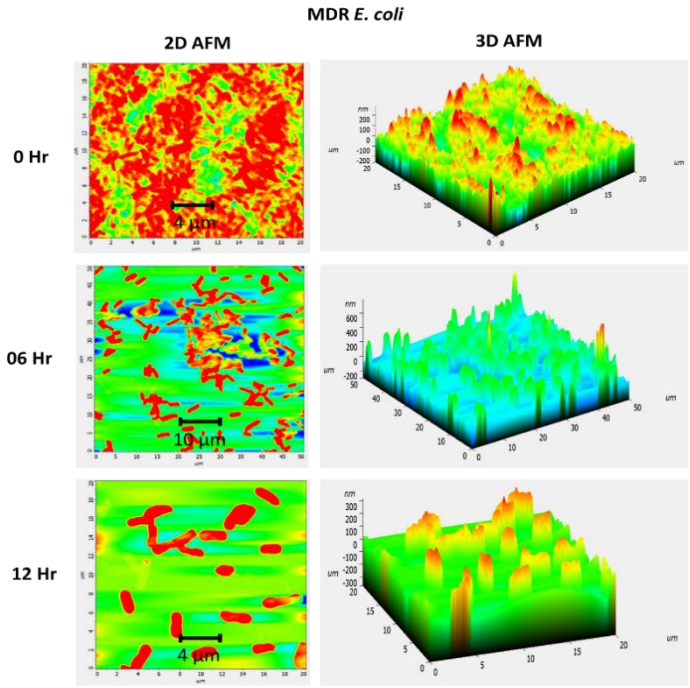

Figure 4.15. Atomic force microscopy study of MDR *E. coli.* after treatment with Au-Ag-TMC-NPs at different interval of time.

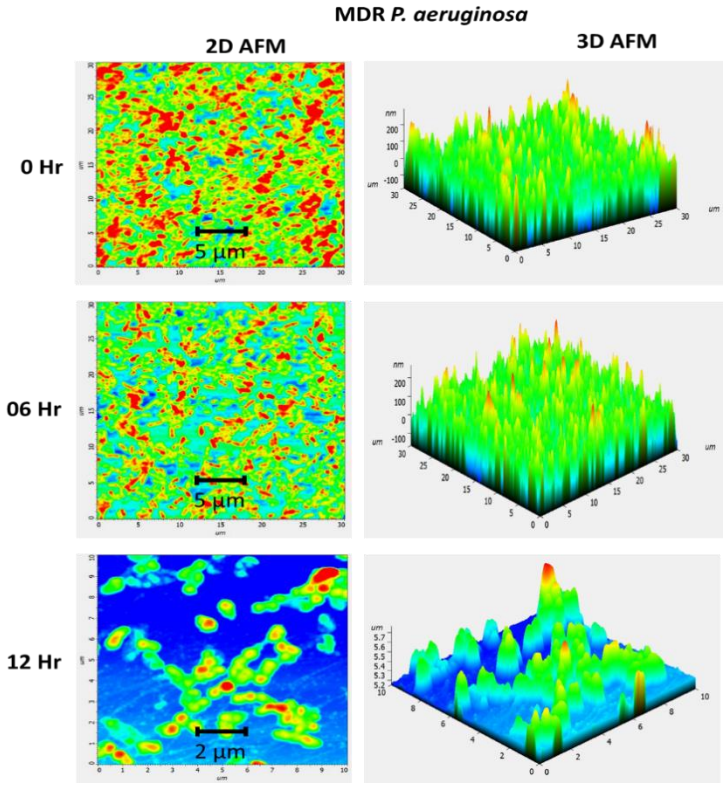

Figure 4.16. Atomic force microscopy study of MDR *P. aeruginosa* after treatment with Au-Ag-TMC-NPs at different interval of time

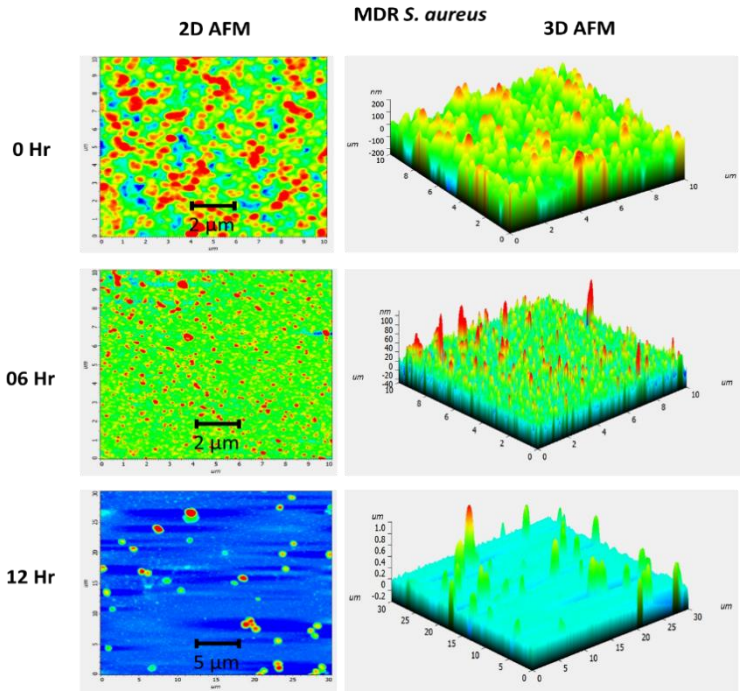

Figure 4.17. Atomic force microscopy study of MDR *S. aureus* after treatment with Au-Ag-TMC-NPs at different interval of time.

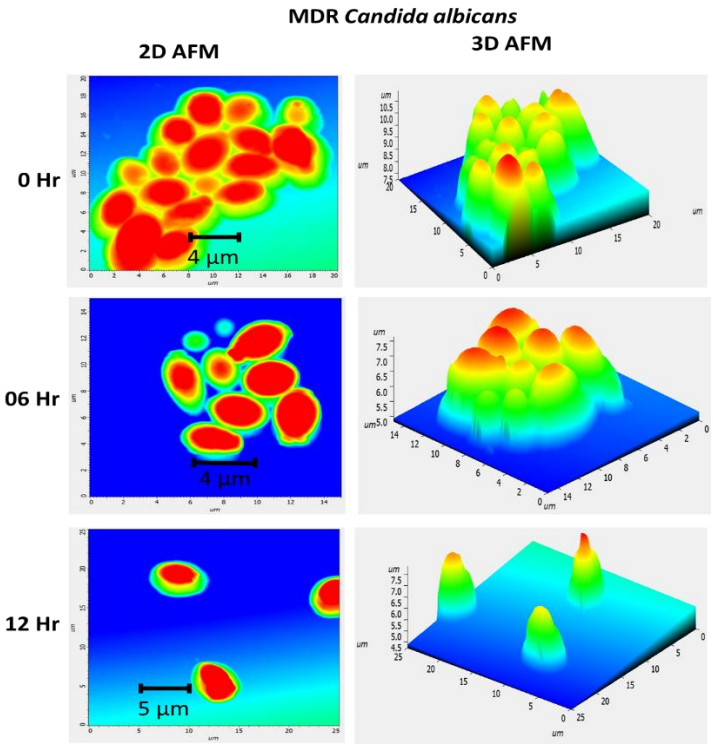

Figure 4.18. Atomic force microscopy study of MDR *C. albicans* after treatment with Au-Ag-TMC-NPs at different interval of time.

4.3.2.5. TEM microscopy study of test microbes

TEM microscopy investigation demonstrated that Au-Ag-TMC-NPs had time-dependent antibacterial activity against MDR microbial strains (**Figure 4.19.**). At 0 h, the MDR microbial strains cell walls were observed to be intact. After 12 h of treatment, the MDR *E. coli.* and MDR *S. aureus* TEM visualization revealed that the cell walls became irregularly wavy, damaged, and the cell wall integrity was lost. Similar results were also observed in a recent study. The TEM visualization of MDR *P. aeruginosa* surprisingly showed the absence of any disturbance in the external membrane but instead unveiled the condensation of DNA inside the bacterial cells. The integrity of the MDR *C. albicans* cell wall is found to be intact, accompanied by alterations in the cellular composition. The study's findings demonstrated that Au-Ag-TMC-NPs has the ability to effectively neutralise

MDR microbial strains by damaging the cell wall integrity, by external membrane disturbance or by bacterial DNA condensation.

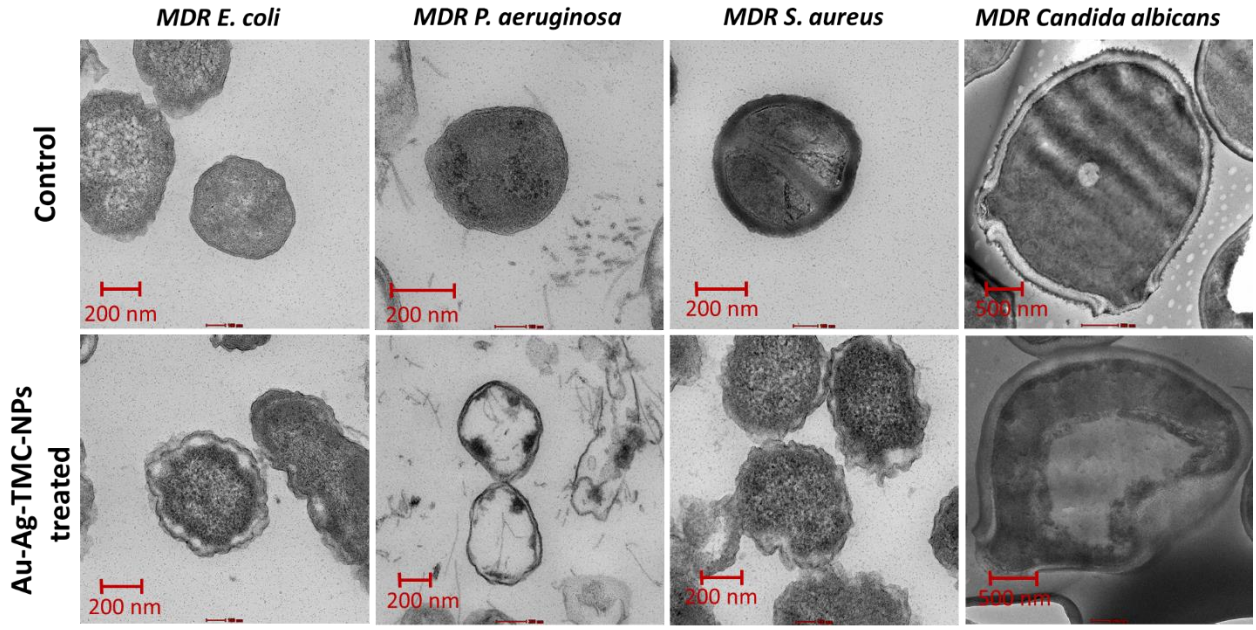

Figure 4.19. Transmission electron micrograph of MDR microbial strains of Au-Ag-TMC-NPs treated and control

4.3.2.6. Effect on the mRNA expression of biofilm-inducing efflux pump

The gene expression profiling of the efflux pump gene has been depicted in **Figure 4.20.** The increased gene expression of the housekeeping gene *ampC* levels of the efflux pump in regards of all the targeted genes. The expression of *acrA* (67.01 ± 2.94 %) and *acrB* (82.94 ± 3.12 %) genes in MDR *E. coli.* are downregulated. Likewise, the downregulation of *MexA* (23.85 ± 1.47 %), *MexB* (28.13 ± 1.69 %), and *OprM* (31.84 ± 2.51 %) genes level of efflux pump in MDR *P. aeruginosa*. Also, the downregulation of *NorA* (42.75 ± 3.76 %) and *NorB* (57.78 ± 4.12%) genes level of the efflux pump in MDR *S. aureus* are found. In MDR *Candida albicans,* the gene *ERG11* (93.73 ± 4.22%), *TAC1* (84.54 ± 2.17%) showed downregulation of genes expression level. All these efflux pump genes are essential for multidrug resistance in MDR *E. coli.*, MDR *P. aeruginosa*, MDR *S. aureus* and MDR

Candida albicans **(Figure 4.20. A, B)**. The obtained results suggested that potential application of the developed Au-Ag-TMC-NPs formulation for inhibition of the MDR microbial efflux pumps activity. In the domain of MDR microbial strains, the downregulation of specific genes may have considerable repercussions for the organism's physiology and behavior. It may lead to decreased production of certain proteins, potentially reducing the bacterial cell's ability to adapt to its environment, respond to stress, or interact with host organisms in the case of dangerous microbes.

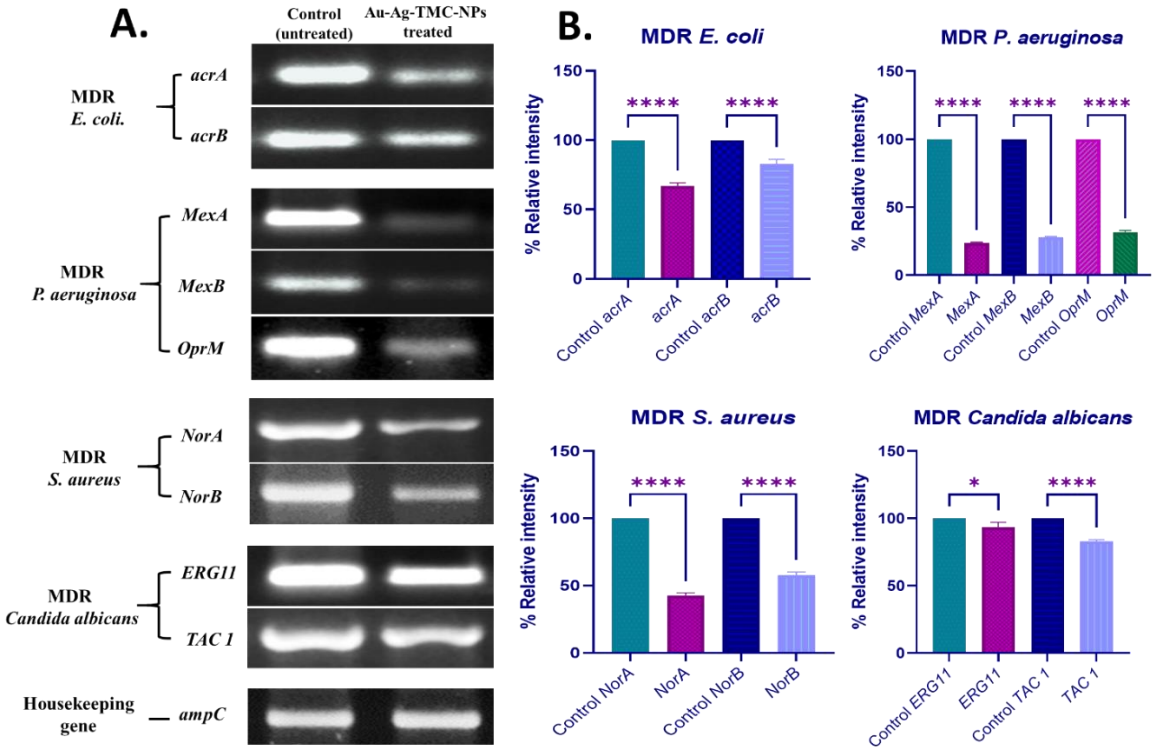

Figure 4.20. (A) Agrose gel electrophoresis of mRNA expressions of different genes on specific MDR microbes showed that the MDR microbes, after treatment with Au-Ag-TMC-NPs showed differential mRNA expression of genes. It was observed that the expression of all the gene was downregulated after treatment with Au-Ag-TMC-NPs except the gene expressions of *ERG11, TAC1* in MDR *Candida albicans* and partially down regulation of *acrA* and *acrB* of MDR *E. coli.* as compared to other expressions of the efflux pump protein (B) Relative % mRNA expression of genes.

4.4. Hemolysis study of nanoparticles

The hemolysis produced by Au-NPs, Au-TMC-NPs, Ag-NPs, Ag-TMC-NPs and Au-Ag-TMC-NPs was compared with distilled water and saline on erythrocytes and was depicted in **Figure 4.21**. The hemolysis (%) induced by distilled water, saline, Au-NPs, Au-TMC-NPs, Ag-NPs, Ag-TMC-NPs and Au-Ag-TMC-NPs was 98.50 ± 1.31%, 1.57 ± 0.11%, 2.94 ± 0.11%, 2.09 ± 0.09%, 3.54 ± 0.14%, 2.10 ± 0.09%, 2.23 ± 0.09%, 1.24 ± 0.05% respectively. According to the findings, the nanoparticles repeatedly shown hemolysis levels that were lower than the predetermined threshold of 2%, which substantiates the fact that they do not display hemolytic properties when they are exposed to human blood.

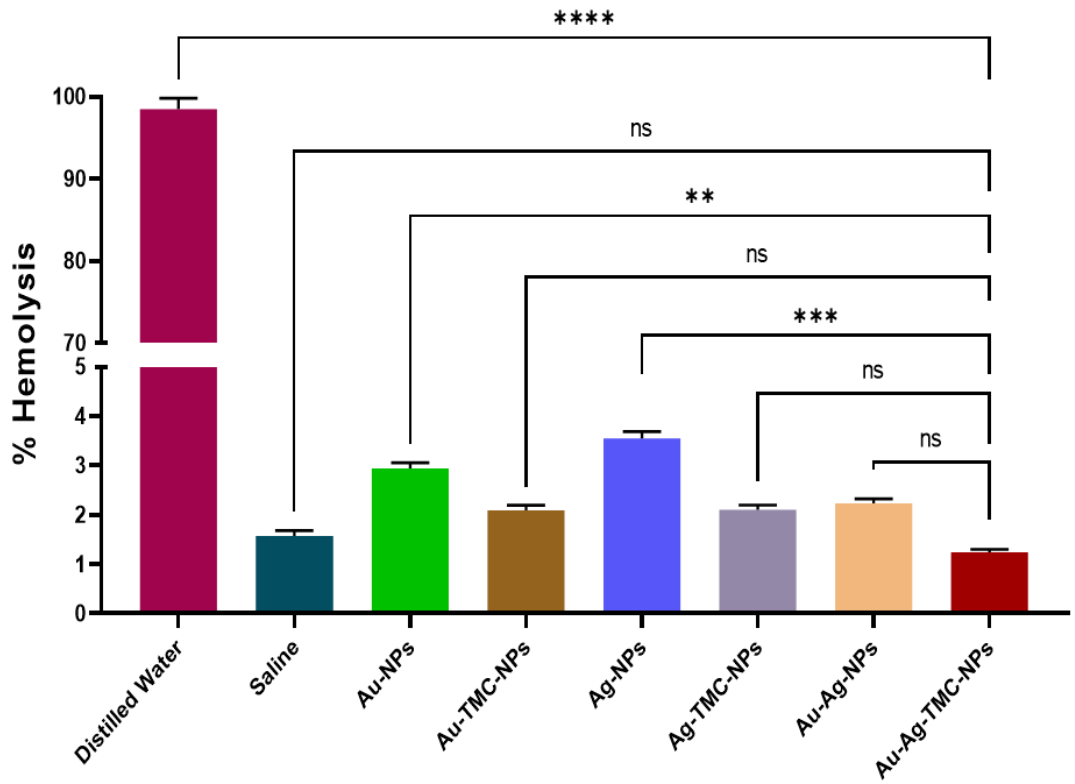

Figure 4.21. Hemolysis of nanoparticles in healthy erythrocytes induced by distilled water, saline, Au-NPs, Au-TMC-NPs, Ag-NPs, Ag-TMC-NPs and Au-Ag-TMC-NPs

4.5. Characterization of nanofibers

4.5.1 Measurement of contact angle

The measured contact angles for blank nanofibers were 36.18 ± 1.64° (left) and 37.52 ± 1.27° (right), whereas the contact angles for Au-Ag-TMC-NPs were 56.54 ± 0.91° (left) and 62.06 ± 1.08° (right) (**Figure 4.22. A, B**). The findings demonstrated that hydrophilicity of the electrospun nanofibers was substantially decreased with the addition of Au-Ag-TMC-NPs in nanofibers.

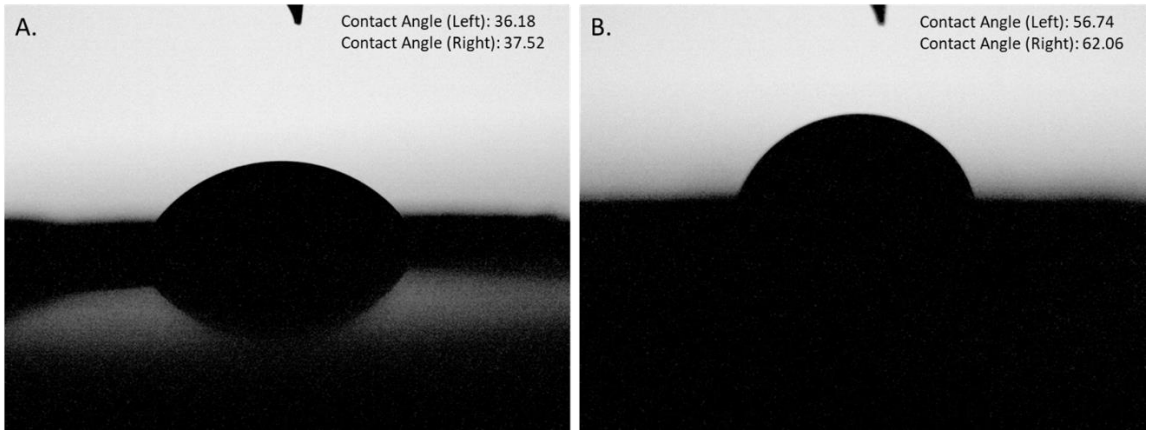

Figure 4.22. Contact angle of A) Blank, and B) Au-Ag-TMC-NPs loaded nanofibers

4.5.2. TEM analysis of Au-Ag-TMC-NPs-NFs

The electron micrograph of the fibers showed the diameter ranged in size (diameter) from 100 nm to 350 nm **(Figure 4.23.).** The TEM study clearly showed the presence of many Au–Ag-TMC-NPs embedded in the nanofibers which can be seen as black spots on the surface of the nanofibers. Within the context of blank nanofibers, the absence of nanoparticles being embedded or trapped within the nanofiber structure is seen. In contrast, the Au-Ag-TMC-NPs-NFs exhibit nanoparticles ranging in size from 50 nm to 110 nm, alongside nanofibers measuring 304 nm in diameter. It was reported that the diameter of the electrospun nanofibers was dependent on the properties of the electrospinning solution, such as viscosity, electrical conductivity, chemical composition, and molecular weight of

the constituent polymers. This observation provides evidence for the existence of Au-Ag-TMC-NPs within the nanofibers.

4.5.3. SEM analysis of Au-Ag-TMC-NPs-NFs

The morphological analysis indicates the presence of a uniform or homogenous network composed of cross-linked nanofibers, with sizes ranging from 100 to 400 nm **(Figure 4.23.).** The material exhibited a persistent and intricate network architecture characterised by interconnected pores in three dimensions in both cases. This finding demonstrated rougher interface architecture which was ascribed to nanofibers mixed on the pore wall, advantageous to both cell adhesion and proliferation.

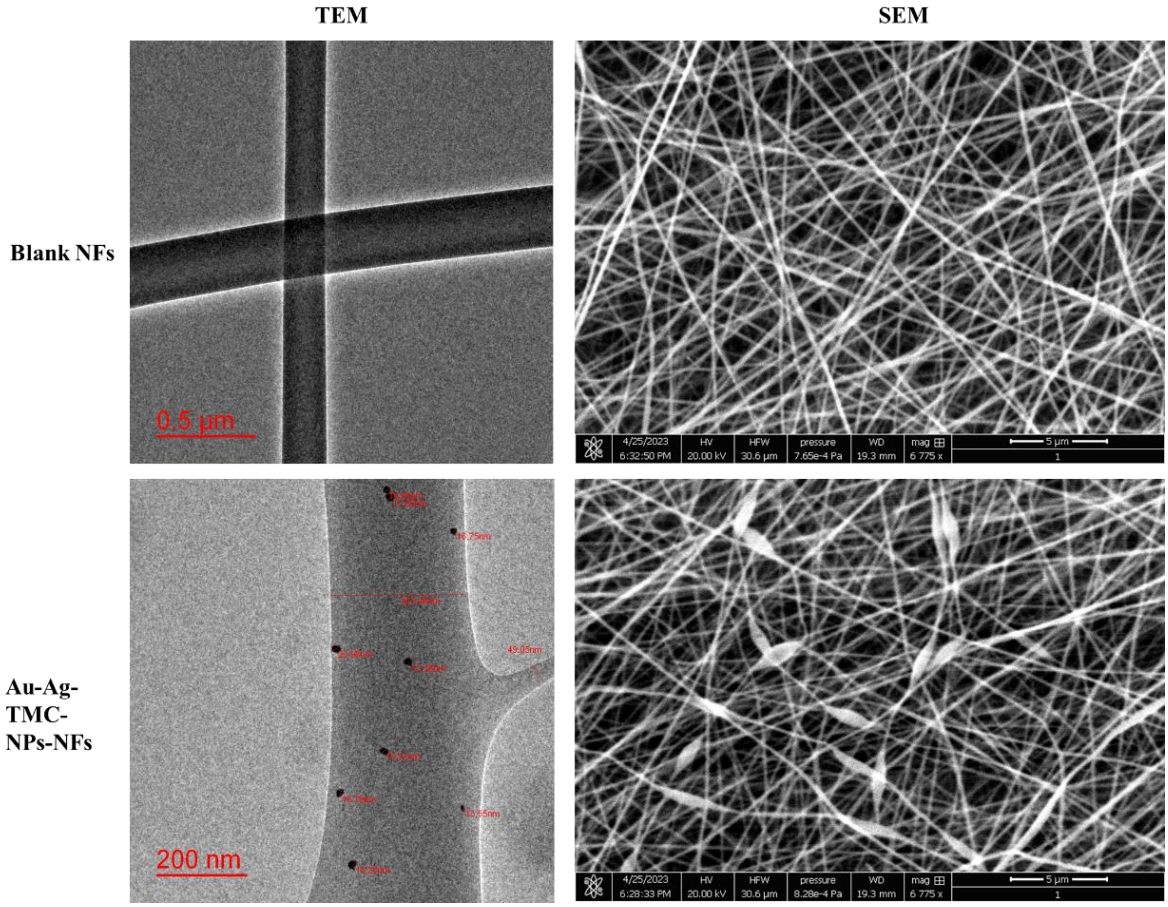

Figure 4.23. TEM and SEM of blank and Au-Ag-TMC-NPs loaded nanofibers

4.5.4. AFM analysis of Au-Ag-TMC-NPs-NFs

The 2D images of the AFM phase and the 3D images of the AFM height were acquired utilizing intermittent-contact (tapping) mode (**Figure 4.24.)**. The samples demonstrated exceptional axial orientation in the fiber architectures, which were characterized by relatively smooth surfaces. No discernible accumulation was detected when Au-Ag-TMC-NPs were adequately situated within the fibers. Furthermore, it has been shown that there are no substantial variations in roughness in either the longitudinal or lateral orientations, indicating that the dispersion of these roughness characteristics within the PVA fibers is satisfactory. The aggregation of certain fibers resulted in the creation of composite structures composed of several fibers. In each instance, the fibers that were prepared resulted in the development of interlaced structures that are accountable for the establishment of quite uniform networks.

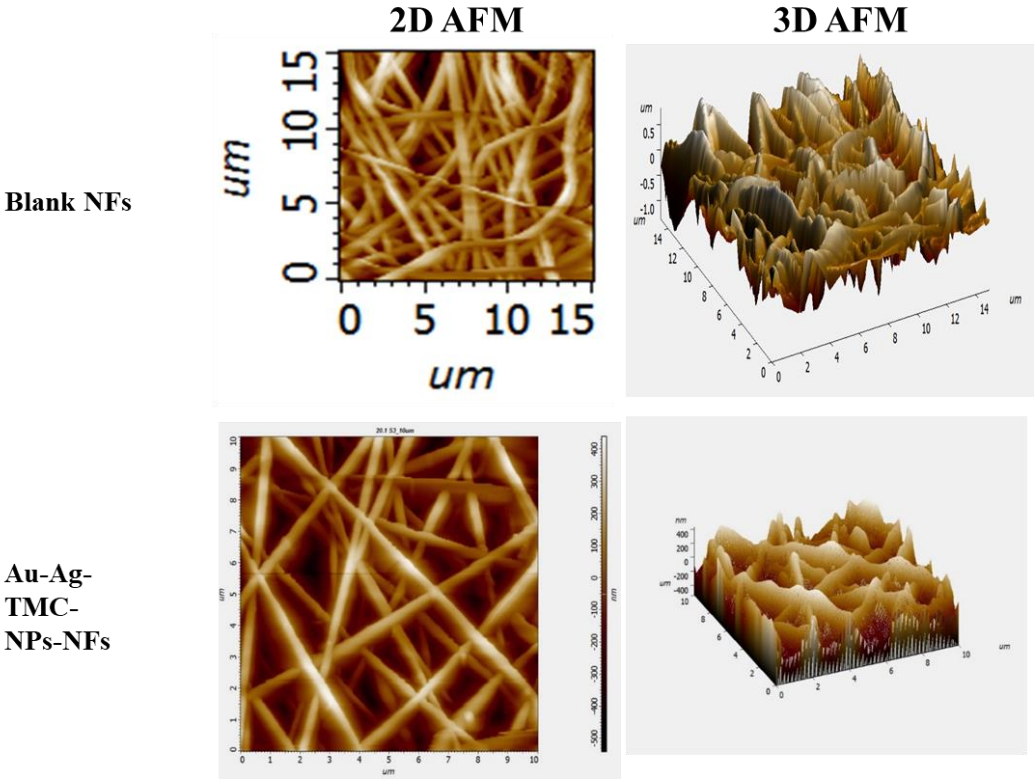

Figure 4.24. 2D AFM and 3D AFM of Blank and Au-Ag-TMC-NPs loaded nanofibers

4.5.5. FT-IR analysis

Broad and prominent peaks about 3400 cm^{-1} were observed for both the samples, corresponding to the stretching vibrations of OH and NH groups (**Figure 4.25.).** The observed phenomenon of the peak's wavenumber shifting towards lower values can be attributed to the increase in PVA/chitosan content within the samples. This shift indicates the formation of hydrogen bonds between the PVA/chitosan and TMC chains. Since PVA contains free hydroxyl group and chitosan has free amine group. So, there will be possibly inter-molecular H-bonding between chitosan and PVA. The weaker N-H vibration corresponding to the peak around 1560 cm^{-1} found in blank nanofiber was suppressed as the PVA content in the samples was increased. This is further evidence that the PVA can crosslink with TMC chains and form hydrogen bonds. PVA/chitosan containing nanofibers' $-CH_2-$ rock band was picked up at 720 cm^{-1}. Additionally, these nanofibers exhibited a peak at 845 cm^{-1} that was associated with C-H bond shaking. By loading the nanoparticles in the blank nanofibers, the samples reduced the absorbance of this peak. Vibration of C-O bonds causes the peak at 1100 cm in PVA-containing nanofibers. Crystallization of PVA is known to affect this shoulder-appearing peak. C-O stretching vibrations are responsible for the peak at 1260 cm^{-1}. PVA's CH-OH and CH_2 symmetric bending mode vibrations peaked at 1370 and 1431 cm^{-1}, respectively.

4.5.6. XRD analysis

XRD is used to analyze the crystallinity in polymeric nanofibers. The XRD spectra of blank fiber showed a broad peak revealing its amorphous nature, whereas the XRD spectra of Au-Ag-TMC-NPs-NF showed sharp peaks at 2θ of 15°, 25° and 28°, which revealed its polycrystalline nature (**Figure 4.26.**). This outcome depicted that the existence of poly-crystallographic orientations inside the nanofiber structure may alter numerous crucial aspects essential to wound healing. For instance, the grain boundaries between crystalline

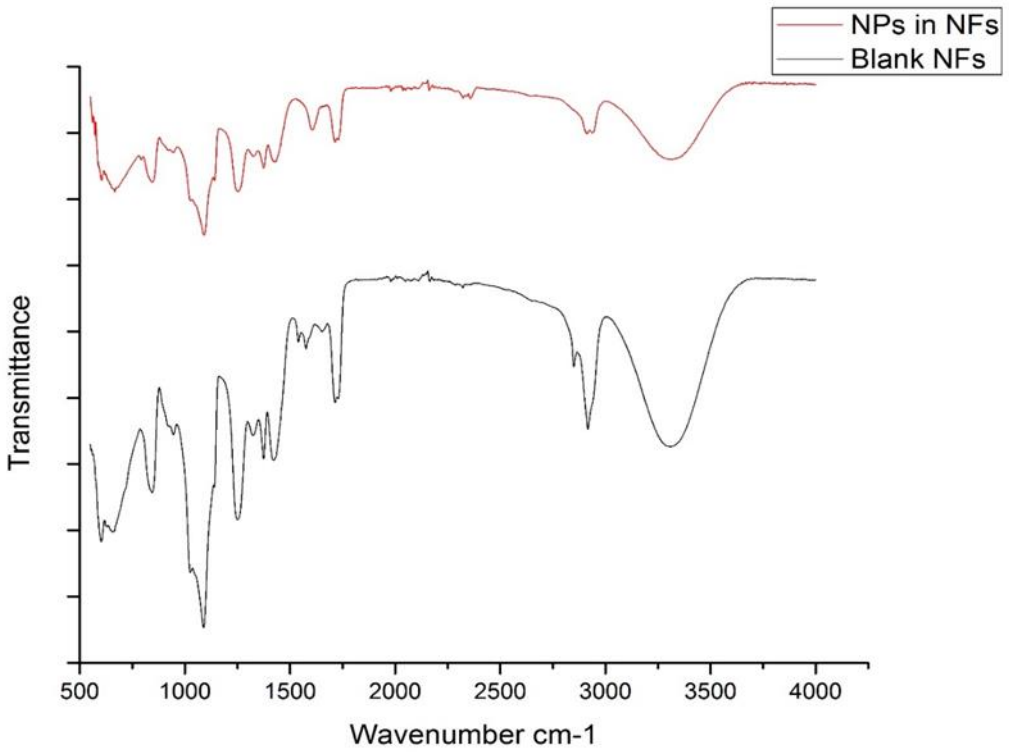

Figure 4.25. FT IR of Blank and Au-Ag-TMC-NPs loaded nanofibers

domains may affect the mechanical characteristics of the nanofibers, influencing their flexibility and strength. This may be critical for ensuring that the nanofibrous material responds efficiently to the dynamic and complicated mechanical environment of the healing wound.

4.5.7. Thermal stability of nanofibers

The degradation temperature of blank nanofiber and NPs in NFs were recorded be 233.54°C and 240.41°C respectively **(Figure 4.27.)**. However, no considerable difference as observed between both the scaffolds, which might be because both have the same outer core material of scaffolds.

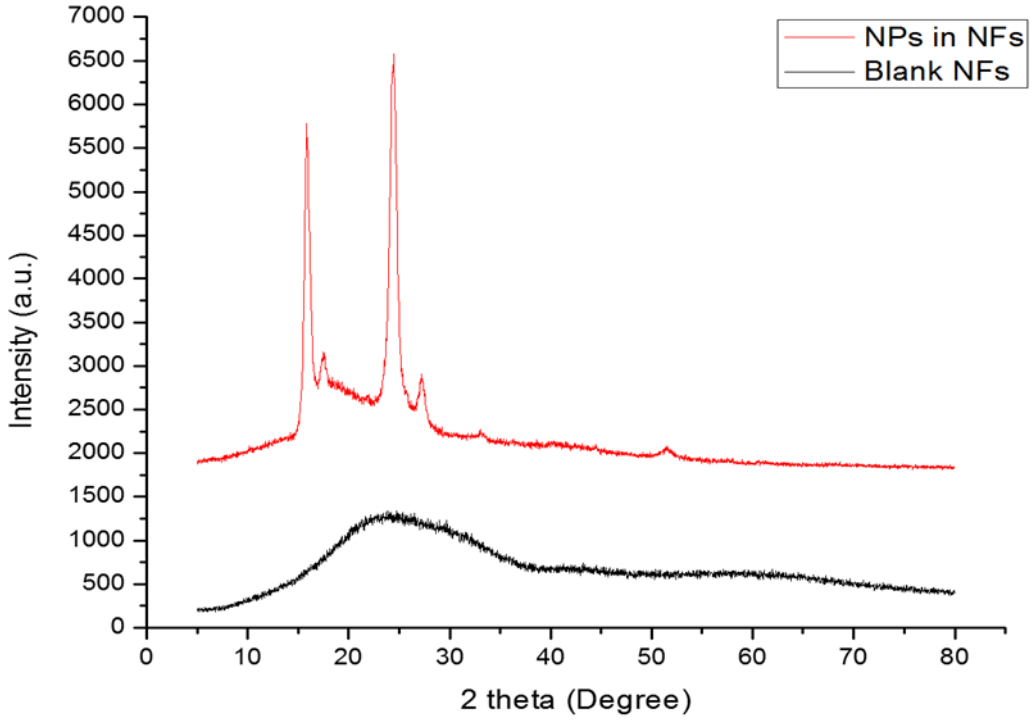

Figure 4.26. XRD of Blank and Au-Ag-TMC-NPs loaded nanofibers

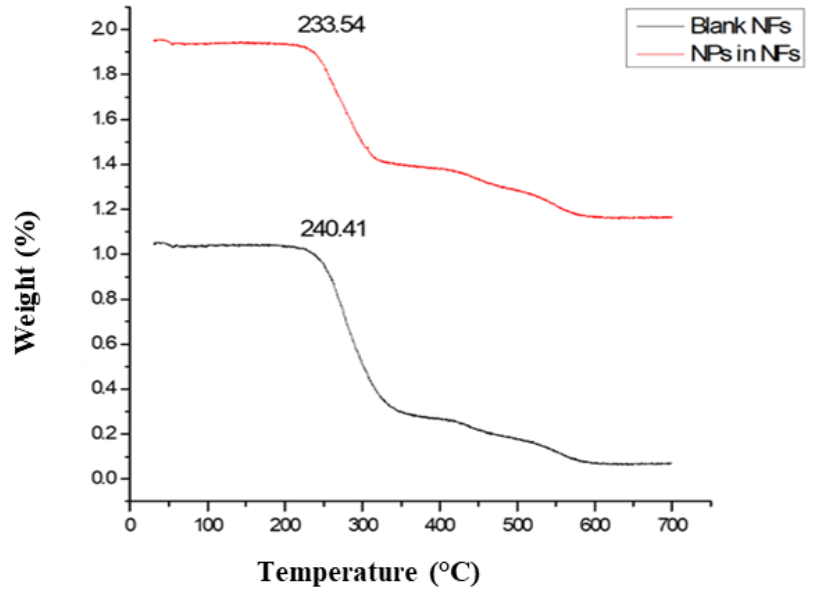

Figure 4.27. Percentage weight loss of the blank and Au-Ag-TMC-NPs loaded nanofibers

4.5.8. Release study of nanofibers

The *in vitro* release profile of Au-Ag-TMC-NPs and Au-Ag-TMC-NPs-NF was found to be 95.19 ± 2.55%, and 25.91 ± 2.12% after 8 h, respectively **(Figure 4.28.)**. The release profile of Au-Ag-TMC-NPs-NFs showed a slow and prolonged release of the Ag^{+} over 48 h, whereas the release profile of Au-Ag-TMC-NPs showed a rapid and complete release of the bimetallic complex within 12 h. These outcomes suggests that Au-Ag-TMC-NPs-NFs has the potential for sustained release of molecules, while Au-Ag-TMC-NPs could be more appropriate for short-term drug delivery.

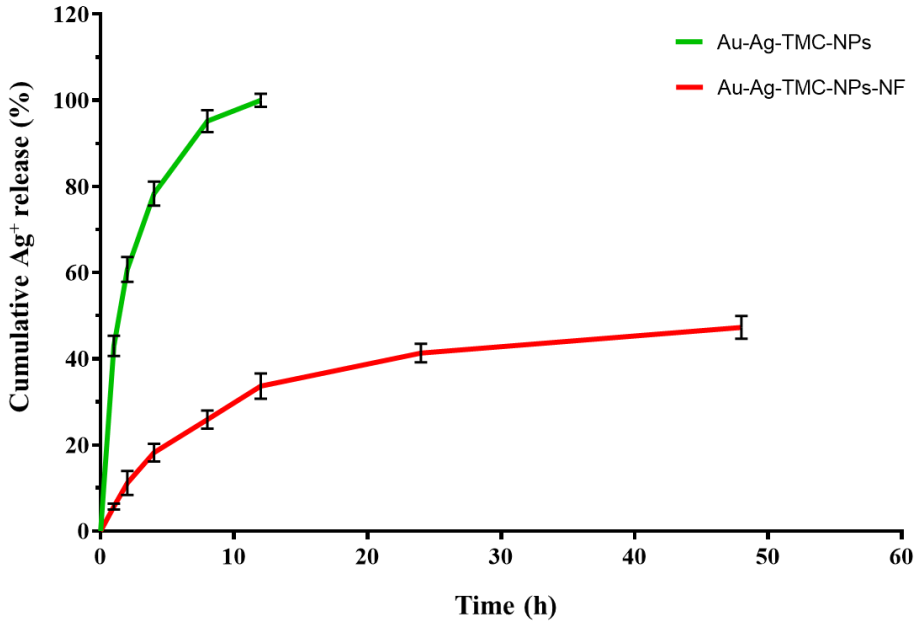

Figure 4.28. Release study of Au-Ag-TMC-NPs and Au-Ag-TMC-NPs-NFs in the PBS (pH-7.4). (n= 3)

4.5.9. Hemolysis study of nanofibers

The percentage of hemolysis induced by distilled water, saline, Au-Ag-TMC-NPs and Au-Ag-TMC-NPs-NFs was 98.53 ± 1.43%, 1.63 ± 0.11%, 1.24 ± 0.05% and 1.01 ± 0.06%

respectively, which indicated that the nanofibers were nonhemolytic in nature. This confirms the nanofibers are considered non-hemolytic materials **(Figure 4.29.)**.

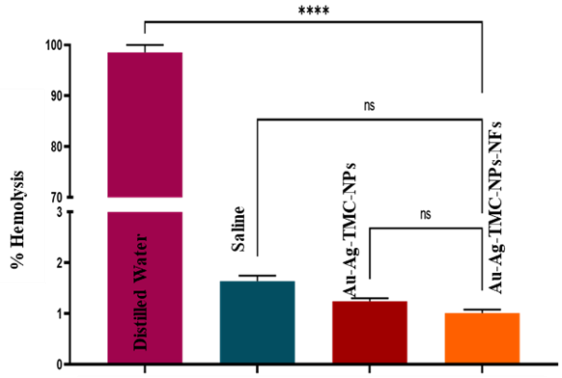

Figure 4.29. Hemolysis of the nanofiber with comparison withg nanoparticles

4.5.10. pH of nanofibers

The dressing pH values of all the blank nanofiber and Au-Ag-TMC-NPs-NFs are 6.95 ± 0.57 and 6.10 ± 0.34 respectively **(Figure 4.30.)**. The nanofibers were designed with an acidic environment to effectively regulate and limit the development of bacteria and the progression of infections. This is because several harmful bacteria flourish in a pH range that is either neutral or slightly alkaline. Additionally, a somewhat acidic pH may facilitate certain elements of the wound healing process, such as the functioning of enzymes responsible for tissue regeneration. Therefore, it was concluded that the acidic Au-Ag-TMC-NPs nanofiber films would furnish an appropriate environment to boost cell proliferation and fibroblast development.

4.5.11. Whole blood clotting ability

The Au-Ag-TMC-NPs-NFs film showed a significantly lower absorbance value than blank nanofiber film as well as pure blood, showed their higher blood clotting ability **(Figure 4.31.)**. Blood clotting ability of nanofiber significantly enhanced after addition of bimetallic nanoparticles.

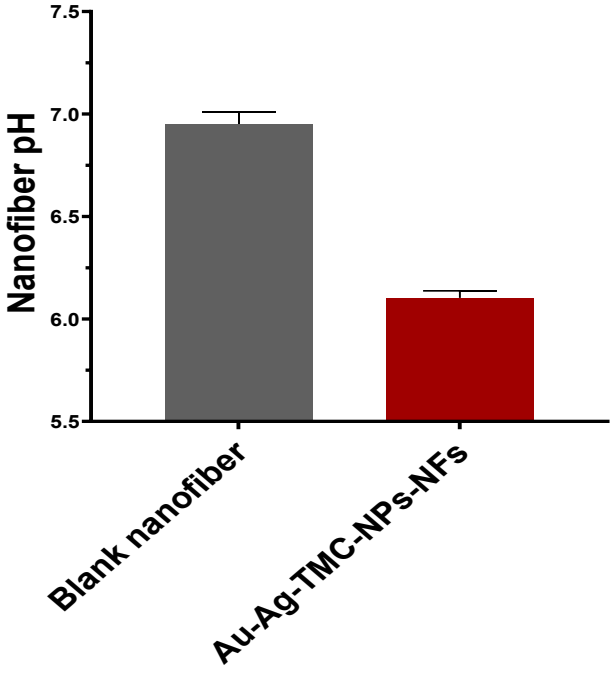

Figure 4.30. pH of the blank and Au-Ag-TMC-NPs loaded nanofibers

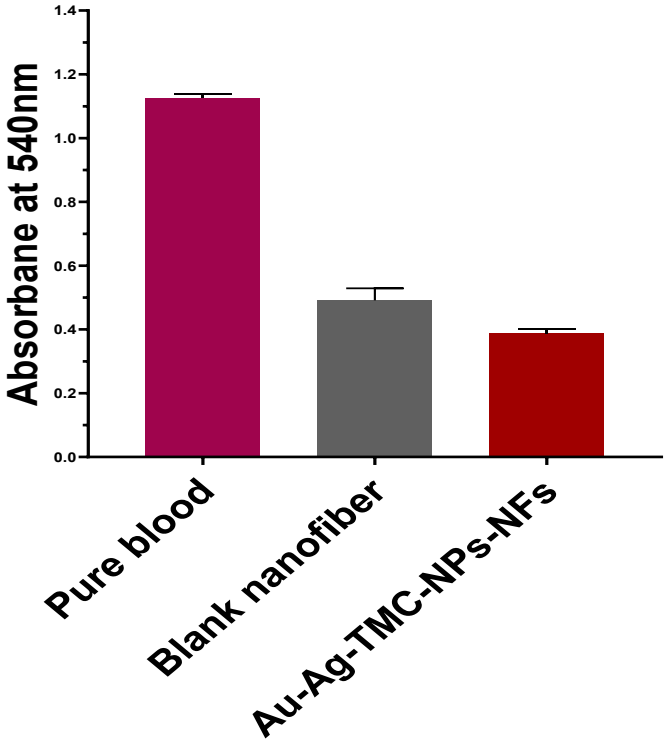

Figure 4.31. The assessment of the coagulation capacity for whole blood of blank and Au-Ag-TMC-NPs-NFs films

4.5.12. Thrombus formation test

Compared to a blank nanofiber film, clot formation was significantly higher when blood met Au-Ag-TMC-NPs-NFs films **(Figure 4.32.)**. Hemostatic assay results showed that the Au-Ag-TMC-NPs-NFs film, with its accelerated blood clotting and thrombus formation abilities, was the most preferable for enhancing hemostasis capabilities.

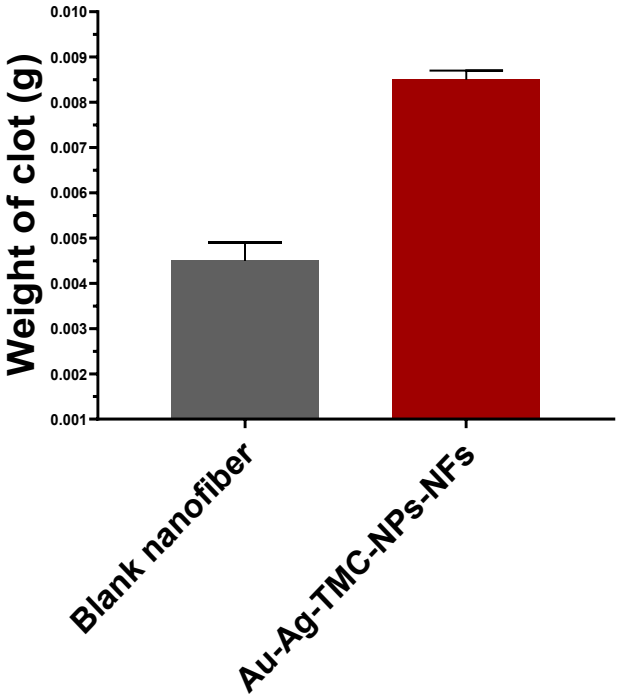

Figure 4.32. Thrombus development of blank and Au-Ag-TMC-NPs-NFs films.

4.5.13. Water retention capacity

The blank nanofiber achieved a weight gain of 713 ± 48% from its initial weight after being merged in PBS solution for 48 h. While the nanoparticles in nanofibers achieved 1137 ± 83% weight gain from its initial weight. Hence it is concluded that the Au-Ag-TMC-NPs-NFs has the highest water retention property among them. Since nanofibers have water retention capacity, it signifies that these nanofibrous materials possess the ability to absorb and retain water or aqueous solutions. This property is very essential in wound healing applications.

4.5.14. Stability and degradation studies of nanofibers

Stability and degradation of nanofiber was done after 13-days of continuous immersing in PBS. The electrospun nanofibers were found to be stable and show no appreciable degradation. Forceps were still able to grip samples after 10 days of continuous immersing in water. Due to the presence of lysozyme in many bodily fluids, including tears and serum, an *in vitro* degradation study was performed to mimic the behavior of nanofibers *in vivo*. Moreover, we found the percentage weight loss in both the nanofibers scaffolds. In particular, blank nanofiber and Au-Ag-TMC-NPs-NFs showed a percentage weight loss of 31.26 ± 1.14 and 8.37 ± 0.53 respectively. This demonstrates the biological stability of the nanofibers to assure compatibility with live tissues and cells, preventing undesirable responses or disintegration.

4.6. Wound healing potential study of Au-Ag-TMC-NPs-NFs

The wound healing activity of Au-Ag-TMC-NPs-NFs was recorded upto day 12 as day 1, day 4, day 8, day 12. There was an observation made that untreated mice wounds showed unhealed **(Figure 4.33.)**. Au-Ag-TMC-NPs-NFs accelerated the wound closure in the group which is infected by MDR *P. aeruginosa* followed by uninfected wound + Au-Ag-TMC-NPs-NFs then *E. coli.* infected + Au-Ag-TMC-NPs-NFs then uninfected + marketed formulation followed by *S. aureus* + Au-Ag-TMC-NPs-NFs and in infected group the delayed healing is observed in *Candida albicans* infected wound treated by Au-Ag-TMC-NPs-NFs, further this investigation is supported by the histopathological study of wounds **(Figure 4.34.)**. The fastest wound healing percentage rate is 99.34 of MDR *P. aeruginosa* infected wound treated by Au-Ag-TMC-NPs-NFs. Therefore, the Au-Ag-TMC-NPs-NFs+ MDR *P. aeruginosa* infected wound healing efficacy in comparison to the other groups. The wound healing process exhibits variations in response to distinct bacterial strains, as

the onset of chronicity in wounds is initiated by the sustained presence of specific bacteria at the tissue level. Particularly, the production of endotoxins contributes to an extended elevation of proinflammatory cytokines such as interleukin-1 and tumor necrosis factor-α. Consequently, this condition leads to heightened levels of matrix metalloproteases and diminished levels of their tissue inhibitors, accompanied by a reduced production of growth factors. While inflammation is a inherent component of the wound healing mechanism, an excessively heightened inflammatory response can protract the repair process. Bacteria indeed play a significant role in facilitating a controlled inflammatory response during the normal process of wound healing. Subinfective levels of bacteria seem to expedite the healing of wounds and the development of granulation tissue. This acceleration is characterized by heightened infiltration of neutrophils, monocytes, and macrophages, elevated levels of prostaglandin E2, and an augmentation in collagen formation.

Furthermore, there have been reports indicating that the integration of metallic nanoparticles into the polymeric matrix of TMC has shown a significant inhibitory impact on bacterial growth [158]. The antibacterial impact of metallic nanoparticles and their associated ions primarily involves the disruption of biofilm components and their structural integrity and the inhibition of bacterial metabolism via several mechanisms. It signifies that these Au-Ag-TMC-NPs nanofibrous materials, presumably functioning as wound dressings or scaffolds, display powerful antimicrobial activities, especially against MDR strains that have gained resistance to several drugs. The integration of TMC and silver nanoparticles into nanofibers boosts their antibacterial activity, and this has numerous implications for wound care applications. Also, this approach has proven the novelty to improve wound healing without any unwanted consequences.

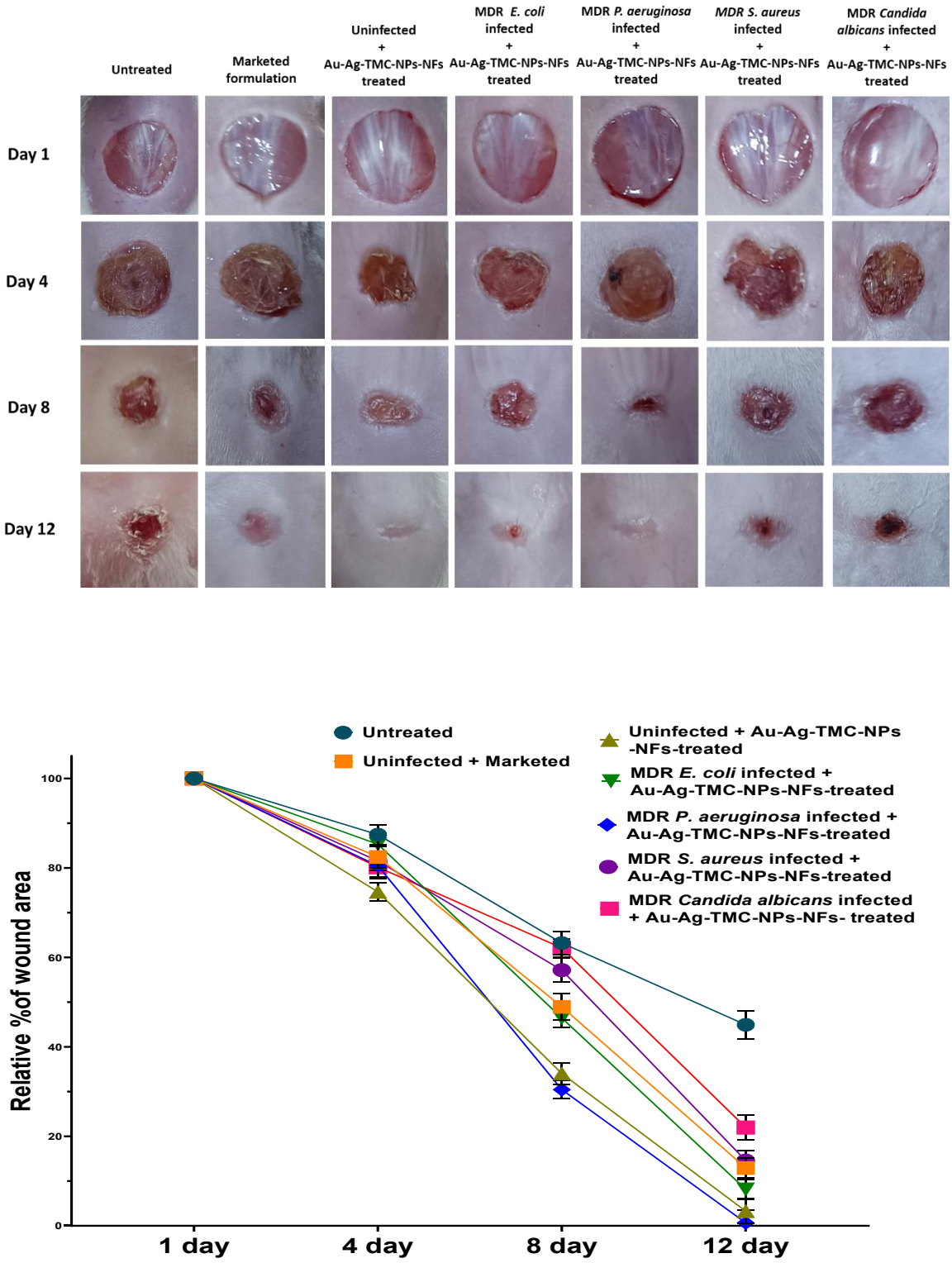

Figure 4.33. Wound healing study signifies that these Au-Ag-TMC-NPs nanofibrous materials, functioning as wound dressings, display powerful antimicrobial activities, especially against MDR strains that have gained resistance to several drugs. Statistical significance among groups was calculated by t-test (n= 5)

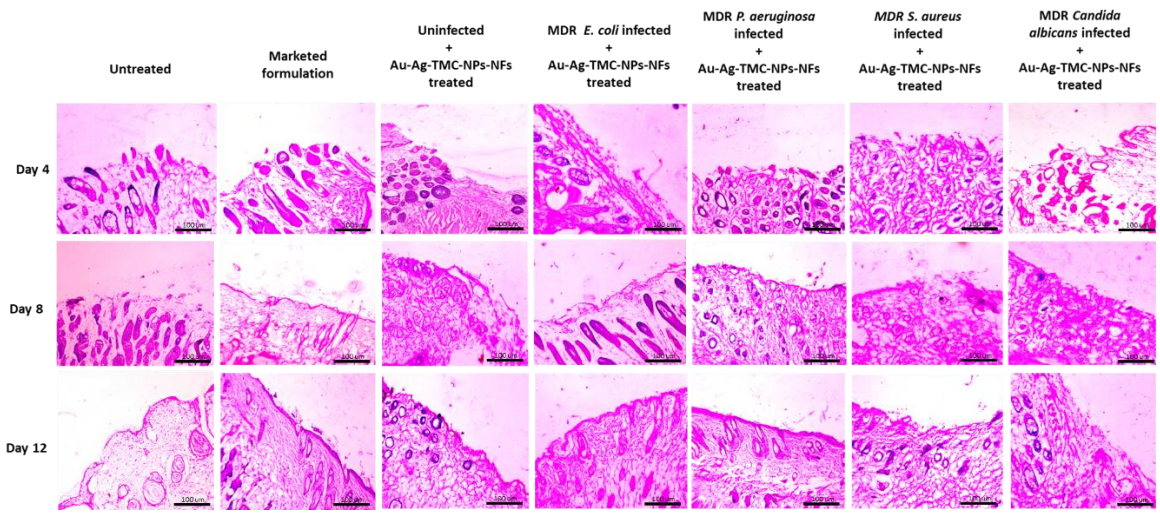

Figure 4.34. Histopathology of wounds of different treatment group of animals under brightfield microscope (at 100× magnification) 4th day, 8th day and 12th day.

4.7. Western blot study of wound healing marker protein

Healing of the wound requires re-epithelialization that involves proliferation along with migration of the epidermal keratinocytes that surround the wound. To migrate over the wound these keratinocytes undergo an epithelial-to-mesenchymal transition (EMT) process, which is characterized by a phenotypic change of the adherent epithelial cells to a dynamic state. These include the re-organization of the cytoskeleton, the decrease in the expression of epithelial junctional components, and the increase in the expression of genes responsible for facilitating cytoskeletal modifications and adhesion to mesenchymal cells [159, 160]. To study the process of wound healing via EMT upon application of Au-Ag-TMC-NPs-NFs, we checked the expression of the mesenchymal marker Vimentin by western blotting **(Figure 4.35.)**. Vimentin is an intermediate filament that has been reported in various studies to be consistently upregulated during the process of EMT. Further, it is one of the robust markers having prognostic values to indicate EMT. Protein lysate was prepared from the wound skin tissues of uninfected mice, and microbial infected mice (MDR strains of *E. coli., P. aeruginosa, S. aureus, and C. albicans*) treated with Au-Ag-

TMC-NPs-NFs. Protein lysate from untreated mice, and mice treated with marketed formulation served as the control samples. The expression of Vimentin was found to be significantly upregulated in wounds of *P. aeruginosa* infected mice treated with Au-Ag-TMC-NPs-NFs compared to the untreated control sample. Vimentin expression was also found to be increased in wounds of MDR *E. coli.* infected and uninfected mice treated with the nanoparticle, whereas samples from MDR *S. aureus* and *C. albicans* infected mice upon treatment with the nanoparticle showed no to very mild expression of Vimentin. Mice treated with marketed formulation also showed a significant expression of Vimentin. Our observations suggested that the application of Au-Ag-TMC-NPs-NFs accelerated wound healing via EMT in MDR *P. aeruginosa*, MDR *E. coli.* infected and uninfected mice as evident from the increased expression level of Vimentin in these protein samples.

Transforming growth factor-beta (TGF-β) signaling has been acknowledged to be a key player in inducing EMT during wound healing and keratinocyte migration. Activation of TGF-β leads to the phosphorylation of downstream signaling molecules SMAD2/3 that subsequently leads to transcription of genes involved in cell proliferation and migration. TGF-β signaling has been reported to induce the expression of Vimentin, thereby leading to the process of EMT. To determine the status of TGF-β signaling known to promote EMT, we assessed the expression status of its downstream signaling component phosphorylated SMAD2 via western blotting in the mice samples. SMAD2 was found to be highly phosphorylated in *P. aeruginosa* infected mice treated with Au-Ag-TMC-NPs-NFs and mice treated with the marketed formulation. This was evident from the increased expression level of p-SMAD2 in both these experimental samples. Reduced expression of p-SMAD2 was observed in the other samples. Our findings indicated that TGF-β was upregulated in MDR *P. aeruginosa* infected mice treated with Au-Ag-TMC-NPs-NFs. Activation of TGF-

β indicated an accelerated wound healing in MDR *P. aeruginosa* infected mice treated with Au-Ag-TMC-NPs-NFs.

According to various studies, it is now established that signaling pathways cross-talk extensively to carry out distinct biological functions. TGF-β has been shown to interact with mitogen activated protein kinases (MAPKs) that regulate the secretion of growth factors and cytokines that promote EMT. MAPKs are protein Ser/Thr kinases that coordinately dictate cell proliferation, differentiation, cell motility and survival. Studies conducted by Davies and the group represents the MAPKs function to enhance SMAD2/3 dependent transcription during TGF-β induced EMT. One of the conventional MAPKs consists extracellular signal-regulated kinases 1 and 2 (ERK1/2). Davies et al demonstrated that MAPKs enhanced SMAD2 dependent transcription leading to promotion of EMT. At this end, phosphorylation of MAPK was more significant in MDR *P. aeruginosa* infected and uninfected mice treated with Au-Ag-TMC-NPs-NFs, as evident from the increased band intensity obtained in these samples compared to other samples. The signaling pathways MAPKs and TGF-β known to regulate EMT have also been suggested to be upregulated in our studies as evident from the expression pattern of p-SMAD2 and p-MAPKs. Here, activation of p-MAPK might indicate a promotion of EMT, thus leading to accelerated wound healing. Our observations suggested that Au-Ag-TMC-NPs-NFs generated in our lab accelerate wound healing in mice via promoting EMT, as evident from the increased expression of the mesenchymal marker Vimentin and this process is being regulated by the activation of the signaling pathways TGF-β and pMAPK (ERK1/2). The **Figure 4.35.** represents the band intensities of Vimentin, p-SMAD2 and p-MAPK in wound inflicted uninfected and microbe infected mice treated with the nanofibers carrying nanoparticles. The untreated mice served as the negative control and the mice treated with marketed formulation served as the positive control. The expression of these markers were

consistently found to elevated in MDR *P. aeruginosa* infected mice treated with Au-Ag-TMC-NPs-NFs. Expression of these markers were observed to be mildly increased in uninfected and MDR *E. coli.* infected mice treated with Au-Ag-TMC-NPs-NFs whereas a negligible expression was observed in mice infected with MDR *S. aureus* and MDR *C. albicans* treated with the nanoparticles. This suggested that the application of Au-Ag-TMC-NPs-NFs generated in our lab-accelerated wound healing in *P. aeruginosa* infected mice. An unpaired t-test was conducted in order to get the p-value (ns-not significant, *p<0.05, **p<0.01, ***p<0.001).

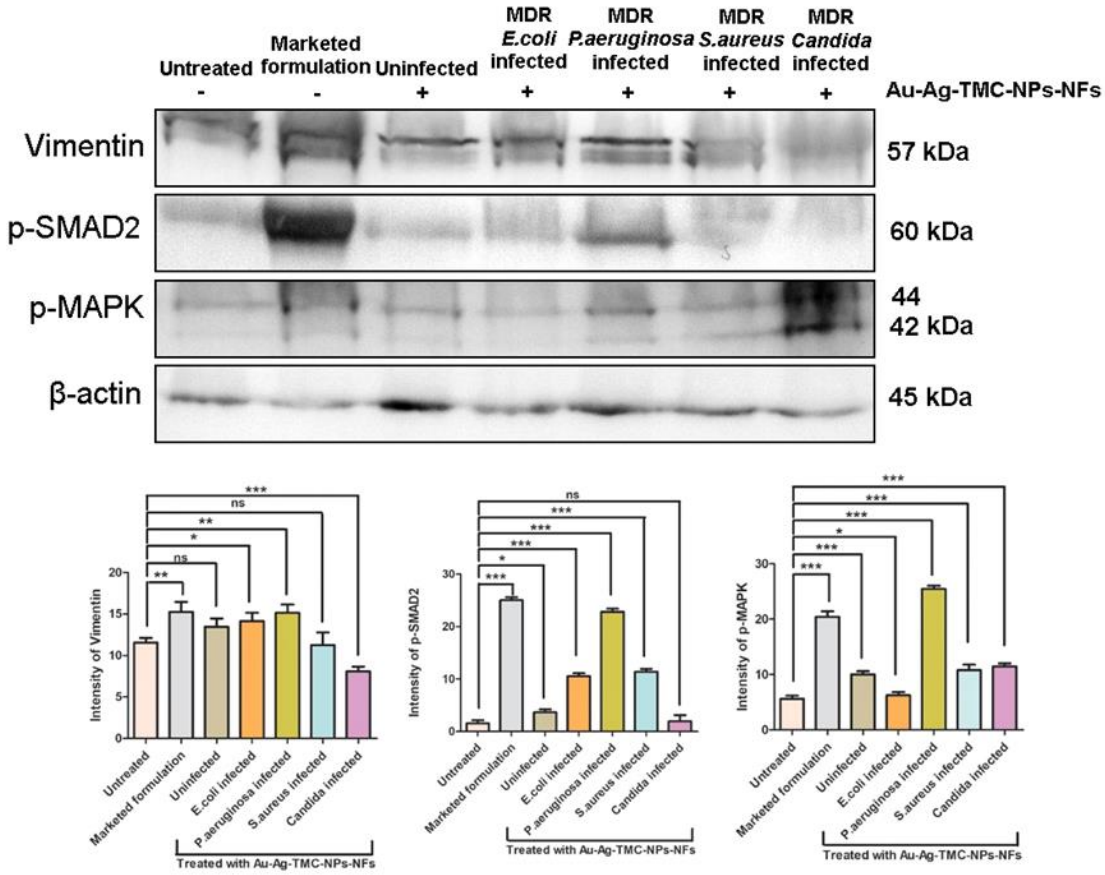

Figure 4.35. Western blotting study **(**A) Au-Ag-TMC-NPs-NFs accelerate wound healing in mice via inducing EMT and activation of TGF-β and ERK pathways (B) Relative % wound marker expressions

4.8. *In vivo* nanoformulation release study

The IVIS study demonstrated the indirect quantification of the rate of biodistribution of nanoparticles over the time. Here, the release of free DiD from blank nanofiber (control) **(Figure 4.36. A)** and Au-Ag-TMC-NPs-NF-DiD **(Figure 4.36. B)** while infected with different microbes within 48h of application. The release was examined at time intervals of 10 min., 1, 2, 4, 8, 24, and 48h post-treatment. The intensity of the DiD dye fluorescence is measured as the radiant efficiency (photons/sec/cm^2/sr). It has been found that DiD is rapidly released from blank nanofiber with free DiD beginning 4h after administration with a significant decrease in the fluorescent signals and disappearing completely 48h later. On the other hand, the nanofibers with DiD tagged nanoparticles (Au-Ag-TMC-NPs-NFs-DiD) exhibited a sustained release of the DiD dye with a slow decrease in fluorescent signals, which provides an understanding of the release of nanoparticles at wound sites over a long period of time with effective treatment. These results confirm the sustained delivery of nanomaterial at infected wound sites over a prolonged period, triggering a positive therapeutic impact **(Figure 4.37. A, B)**.

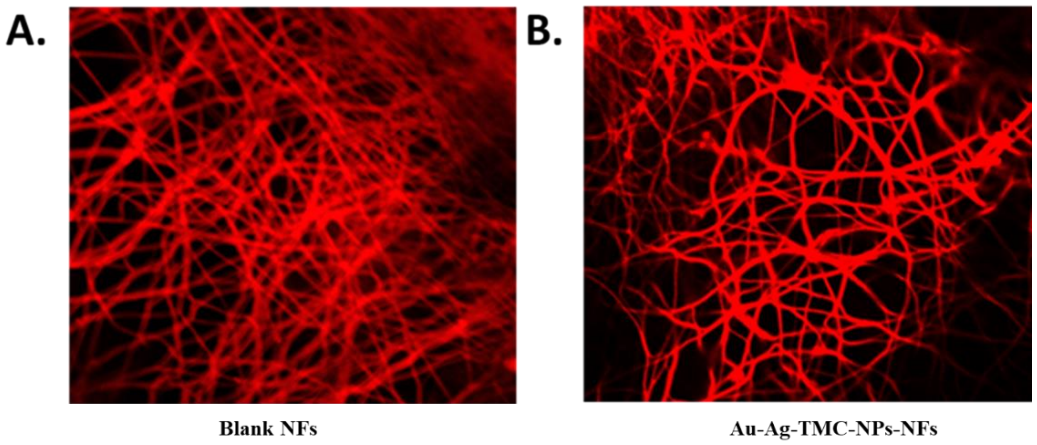

Figure 4.36. CLSM confocal microscopy of A) Free-DiD-blank nanofiber (control) and B) Au-Ag-TMC-NPs-NFs-DiD. (DiD dye= Excitation: 620 nm ; Emission: 710 nm)

4.9. *In vivo* ultrasound/photoacoustic study

Photoacoustic imaging of the MDR microbial infected wound of mice was recorded at day 1 and at 4, 8, and 12 days after treatments **(Figure 4.38. - Figure 4.40.).** The ultrasound/PA images indicated a notable improvement in the healing process of the infected wound following the implementation of nanofibers. The blood flow in all the respective groups was studied by using the power doppler method **(Figure 4.41.).** The percentage vascularity **(Figure 4.43.)** changes on 12^{th} day of infected wound healing were 54.56 ± 2.10, 78.15 ± 1.28, 80.45 ± 1.70, 69.45 ± 2.13, 90.66 ± 2.79, 61.56 ± 1.26 and 57.63 ± 2.78 for untreated, uninfected-marketed, uninfected, MDR *E. coli.* infected Au-Ag-TMC-NPs-NFs treated, MDR *P. aeruginosa* infected Au-Ag-TMC-NPs-NFs treated, MDR *S. aureus* infected Au-Ag-TMC-NPs-NFs treated, and MDR *C. albicans* infected Au-Ag-TMC-NPs-NFs treated groups respectively. Photoacoustic (PA) imaging was used to assess the changes % sO_2 **(Figure 4.42.)**. The sO_2 percentage changes on 12^{th} day of infected wound healing were 51.64 ± 1.60, 65.36 ± 1.78, 69.98 ± 1.70, 65.98 ± 1.64, 77.64 ± 1.43, 61.20 ± 1.26 and 55.17 ± 1.98 for untreated, uninfected-marketed, uninfected, MDR *E. coli.* infected Au-Ag-TMC-NPs-NFs treated, MDR *P. aeruginosa* infected Au-Ag-TMC-NPs-NFs treated, MDR *S. aureus* infected Au-Ag-TMC-NPs-NFs treated, and MDR *C. albicans* infected Au-Ag-TMC-NPs-NFs treated groups respectively. The provided **(Fig. 10C)** displays representative maximum intensity projections of wound healing pictures acquired using 3D power Doppler. The provided photos offer a qualitative representation of the blood flow intensity observed on day 1 and on days 4, 8, and 12 following the therapy. The vascular index was employed to quantitatively assess the relative alterations in blood flow within the wound.

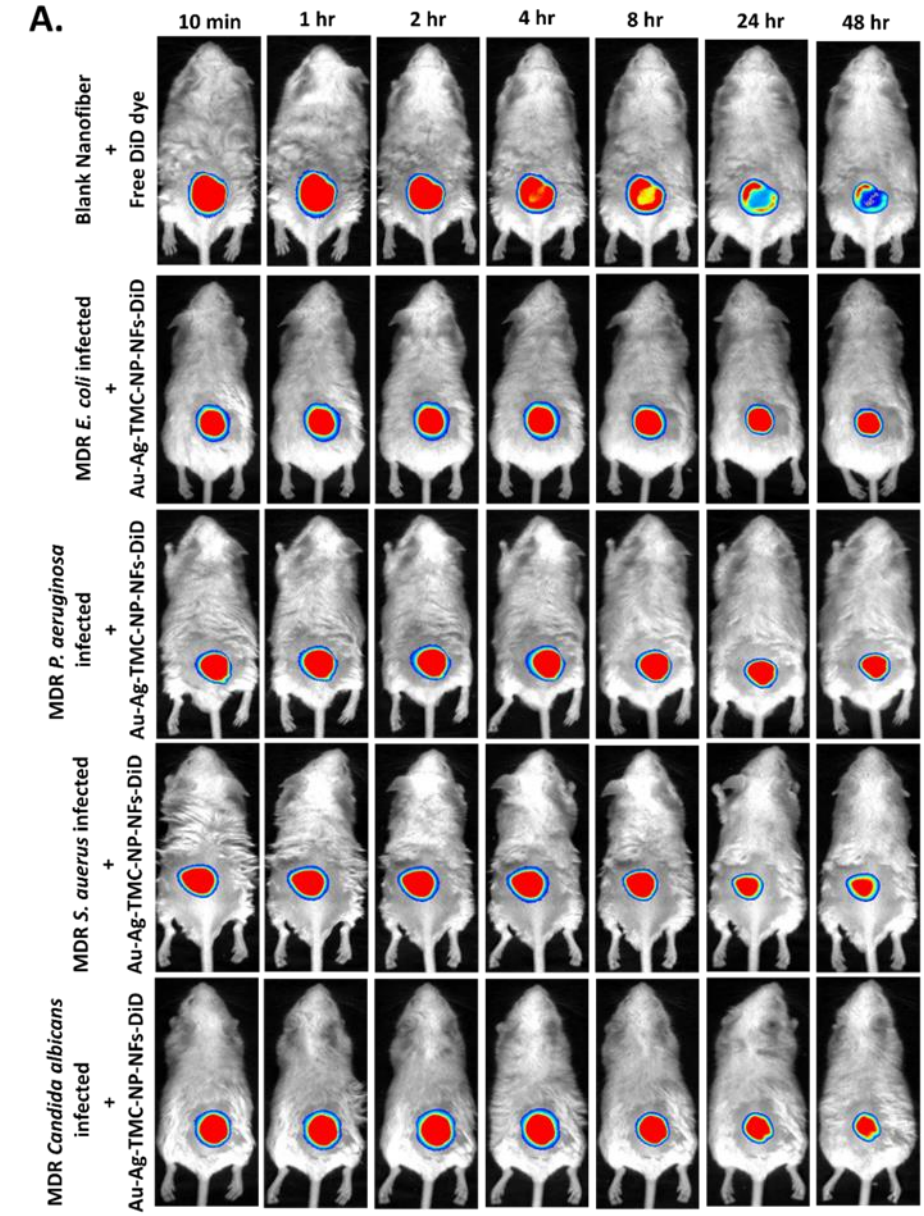
A.
10 min
1 hr
2 hr
4 hr
8 hr
24 hr
48 hr
Blank Nanofiber + Free DiD dye
MDR E. coli infected + Au-Ag-TMC-NP-NFs-DiD
MDR P. aeruginosa infected + Au-Ag-TMC-NP-NFs-DiD
MDR S. auerus infected + Au-Ag-TMC-NP-NFs-DiD
MDR Candida albicans infected + Au-Ag-TMC-NP-NFs-DiD

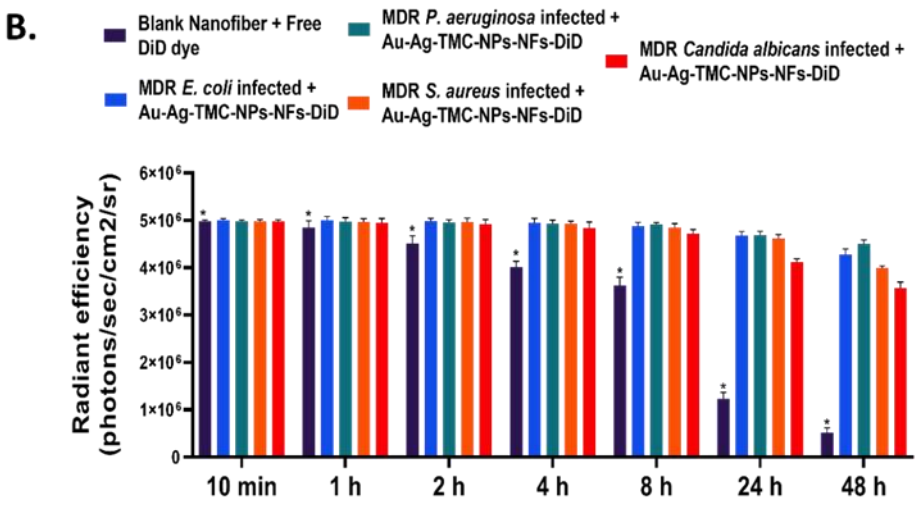
B.
Blank Nanofiber + Free DiD dye
MDR P. aeruginosa infected + Au-Ag-TMC-NPs-NFs-DiD
MDR Candida albicans infected + Au-Ag-TMC-NPs-NFs-DiD
MDR E. coli infected + Au-Ag-TMC-NPs-NFs-DiD
MDR S. aureus infected + Au-Ag-TMC-NPs-NFs-DiD
Radiant efficiency (photons/sec/cm2/sr)
6×10⁶
5×10⁶
4×10⁶
3×10⁶
2×10⁶
1×10⁶
0
10 min
1 h
2 h
4 h
8 h
24 h
48 h

Figure 4.37. *In vivo* live optical imaging (A) *In vivo* biodistribution of free-DiD from blank nanofiber (as control) and Au-Ag-TMC-NPs-NF-DiD while infected with different microbes within 48 h of application at 10 min., 1, 2, 4, 8, 24, and 48h post-treatment (B) CLSM Confocal microscopy of Blank nanofiber + Free DiD dye.

Outcome of *in vivo* ultrasound/photoacoustic study indicates that the rate of wound healing is significantly higher in MDR *P. aeruginosa* infected wounds treated with Au-Ag-TMC-NPs-NFs compared to uninfected wounds. Additionally, the healing rate is higher in uninfected wounds treated with a commercially available formulation compared to MDR *E. coli.* infected wounds treated with Au-Ag-TMC-NPs-NFs. Furthermore, MDR *S. aureus* infected wounds treated with Au-Ag-TMC-NPs-NFs exhibits a faster healing rate compared to MDR *Candida albicans* infected wounds treated with the same nanoparticles. Lastly, the slowest rate of healing is observed in untreated wounds. Because the persistence of certain microbes at the tissue level is what causes wounds to become chronic, the healing process varies depending on the kind of microbial infection present.

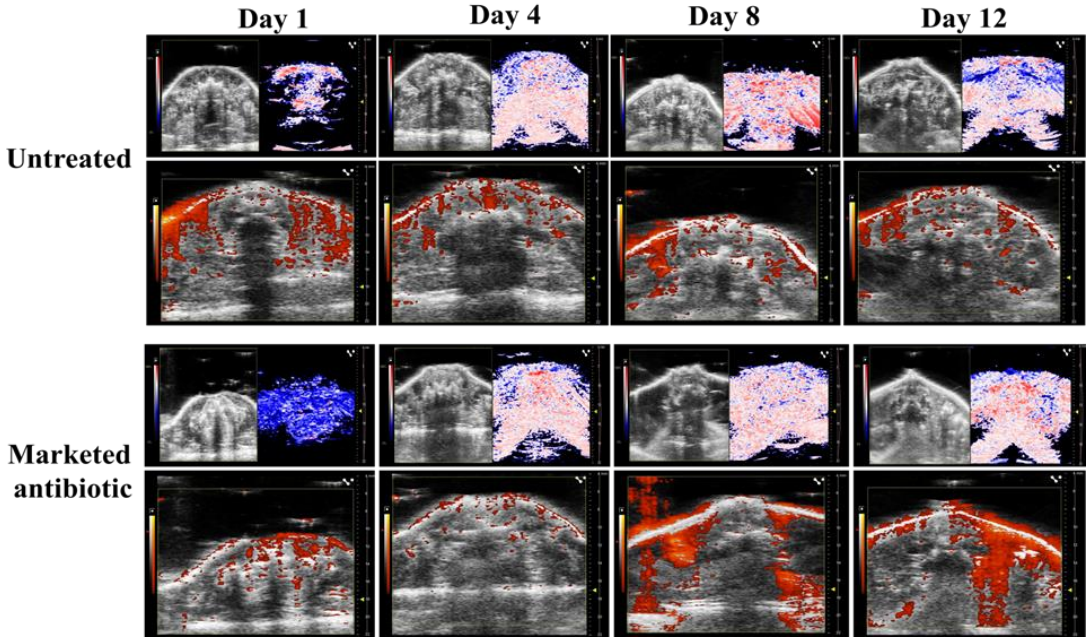

Figure 4.38. PA imaging of untreated and marketed antibiotic

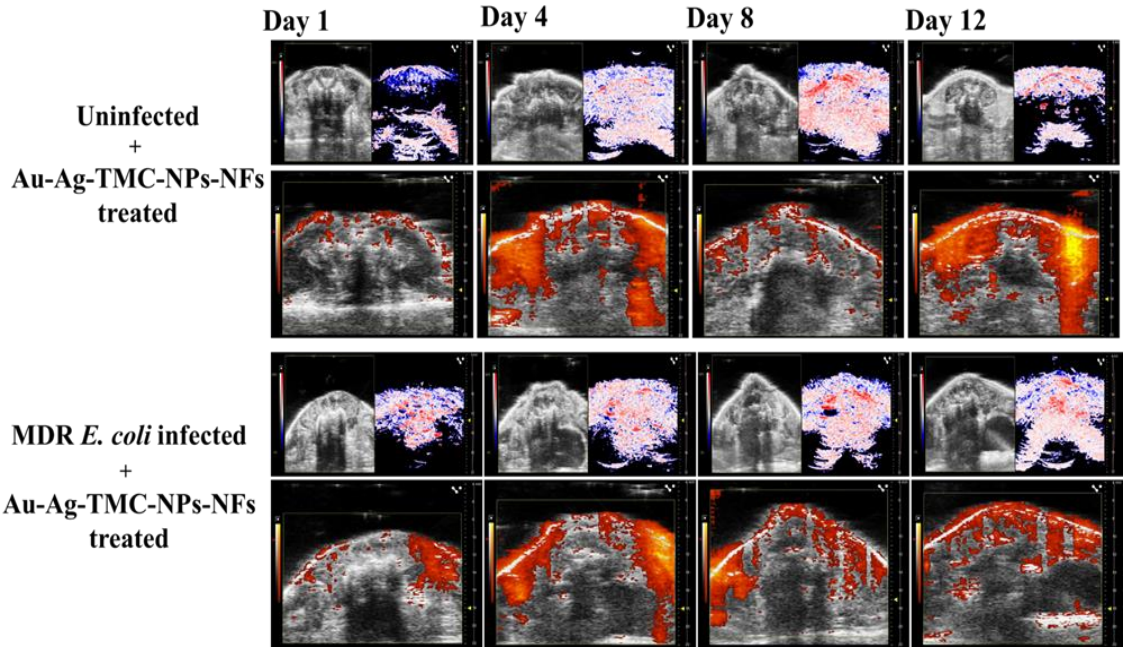

Figure 4.39. PA imaging of uninfected and MDR *E. coli.* infected + Au-Ag-TMC-NPs-NFs

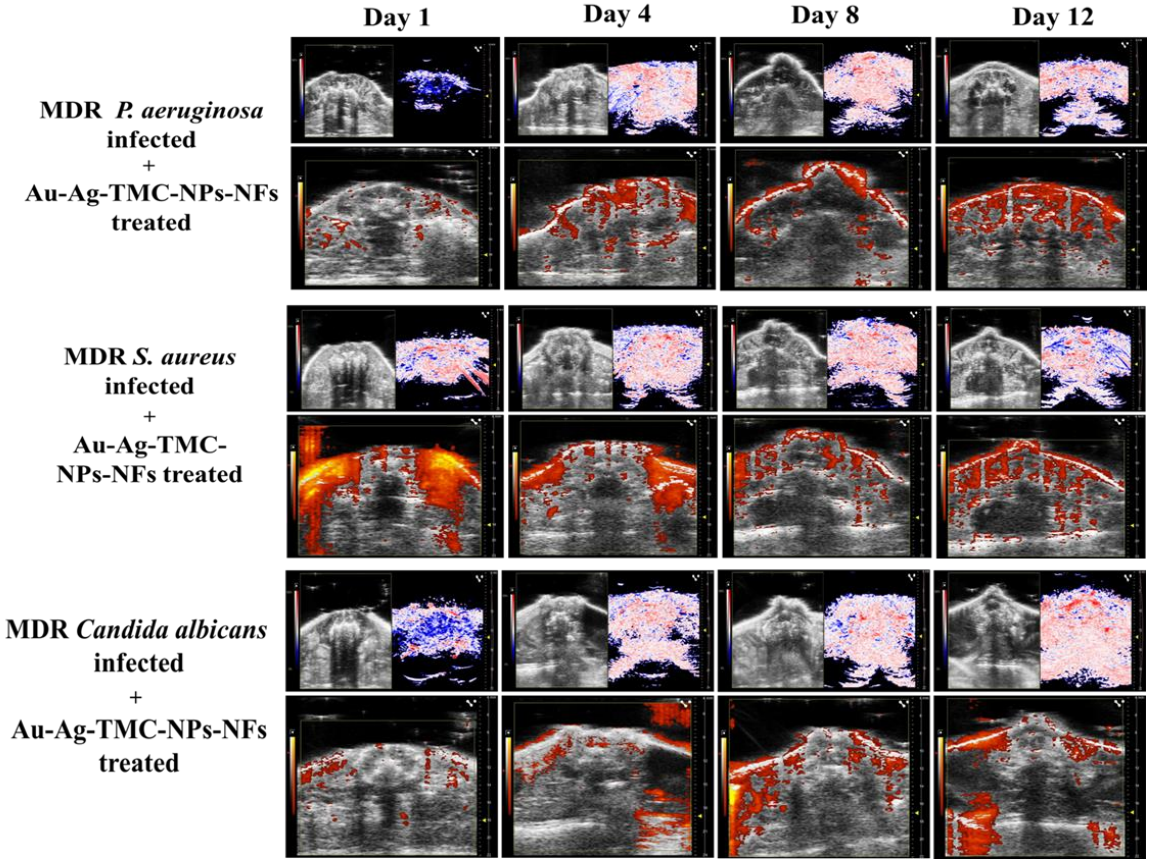

Figure 4.40. PA imaging of MDR *P. aeruginosa*, MDR *S. aureus* and MDR *Candida albicans* infected + Au-Ag-TMC-NPs-NFs

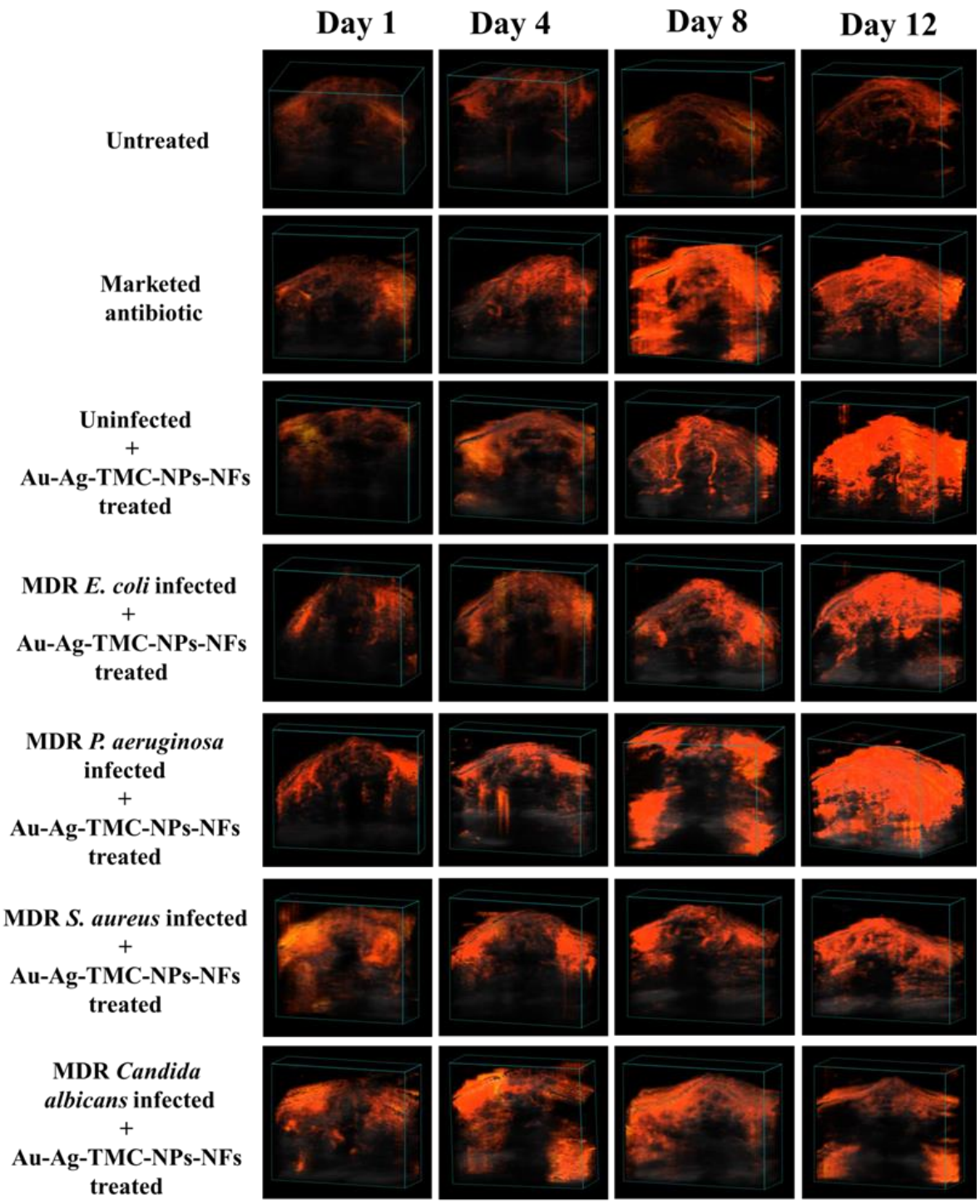

Figure 4.41. Power doppler of uninfected and MDR *E. coli.*, MDR *P. aeruginosa*, MDR *S. aureus* and MDR *Candida albicans* infected treated with Au-Ag-TMC-NPs-NFs

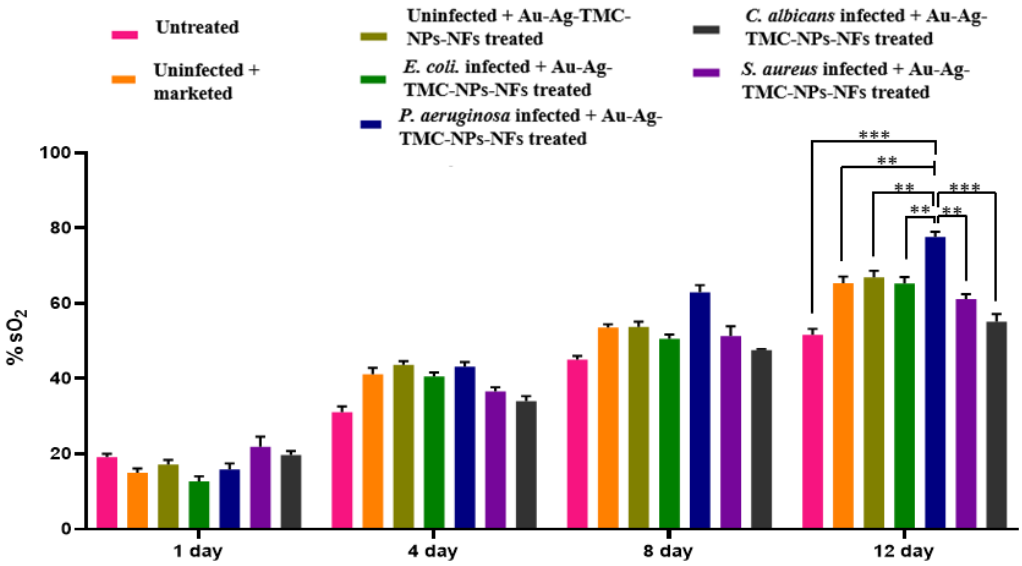

Figure 4.42. Saturated oxygen of uninfected and MDR *E. coli.*, MDR *P. aeruginosa*, MDR *S. aureus* and MDR *Candida albicans* infected treated with Au-Ag-TMC-NPs-NFs Statistical significance among groups was calculated by t-test, (n= 3; the values ns ($p \geq 0.05$), * ($p < 0.05$), ** ($p < 0.01$), *** ($p < 0.001$), and **** ($p < 0.0001$) were considered for significance level determination)

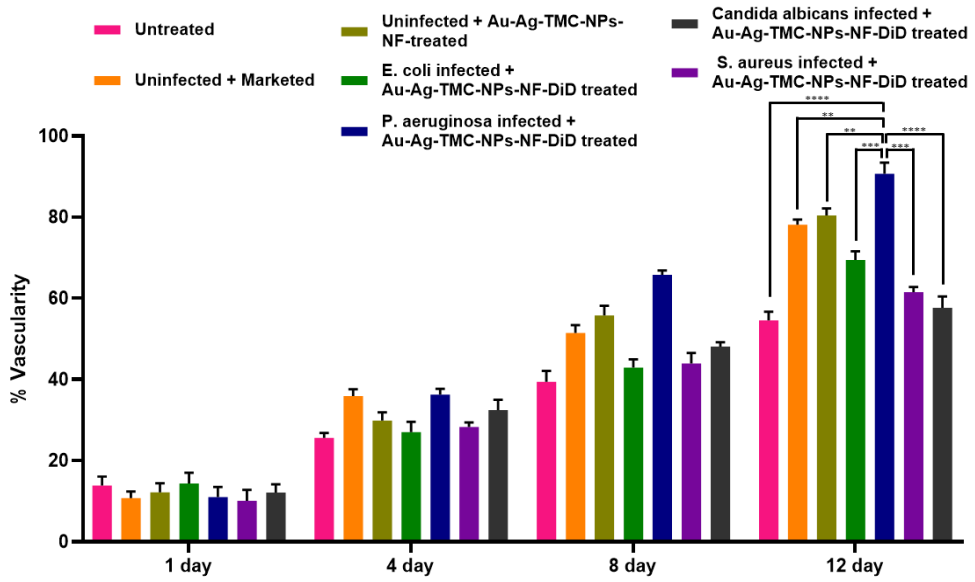

Figure 4.43. Vascularity of uninfected and MDR *E. coli.*, MDR *P. aeruginosa*, MDR *S. aureus* and MDR *Candida albicans* infected treated with Au-Ag-TMC-NPs-NFs; (n= 3; the values ns ($p \geq 0.05$), * ($p < 0.05$), ** ($p < 0.01$), *** ($p < 0.001$), and **** ($p < 0.0001$) were considered for significance level determination)

4.10. Conclusion

This research highlights the remarkable versatility of TMC when combined with bimetallic gold-silver nanoparticles (Au-Ag NPs), demonstrating its potential as a powerful agent for the accelerated healing of wounds infected with MDR microbes, all while avoiding the adverse effects commonly associated with existing commercial wound care formulations. The innovative wound dressing developed in this study, incorporating Au-Ag-TMC-NPs, was shown to effectively downregulate the expression of efflux pump genes in MDR microbes a key mechanism by which these pathogens typically evade antimicrobial therapies. This downregulation is particularly significant, as it suggests a reduction in microbial resistance and an enhanced susceptibility to treatment. The dressing was engineered to provide a sustained and controlled release of therapeutic agents directly at the wound site, resulting in notably accelerated healing with complete wound closure observed within just 12 days. Molecular analyses, specifically western blotting, revealed a pronounced increase in collagen deposition in wounds treated with the Au-Ag-TMC-NPs dressing, indicating not only effective infection control but also robust tissue regeneration and structural repair. In addition, advanced real-time wound assessment using ultrasound and photoacoustic imaging confirmed improved oxygen saturation, increased vascularity, and a greater degree of wound closure, all of which are critical factors in successful wound healing. Future research should aim to explore alternative delivery platforms and expand the investigation to include MDR strains from diverse geographic locations to fully validate and optimize this approach. Overall, the Au-Ag-TMC-NPs-NFs wound dressing not only represents a significant advance in the management of MDR-infected wounds but also lays a strong foundation for the future development of novel antibacterial and antifungal agents with substantial wound-healing potential.